

Mapping dynamical ejecta and disk masses from numerical relativity simulations of neutron star mergers

Vsevolod Nedora¹, Federico Schianchi^{2,1}, Sebastiano Bernuzzi¹, David Radice^{3,4,5}, Boris Daszuta¹, Andrea Endrizzi¹, Albino Perego^{6,7}, Aviral Prakash^{3,4}, and Francesco Zappa¹

¹*Theoretisch-Physikalisches Institut, Friedrich-Schiller-Universität Jena, 07743, Jena, Germany*

²*Institut für Physik und Astronomie, Universität Potsdam,*

Haus 28, Karl-Liebknecht-Str. 24/25, 14476, Potsdam, Germany

³*Institute for Gravitation & the Cosmos, The Pennsylvania State University, University Park, PA 16802, USA*

⁴*Department of Physics, The Pennsylvania State University, University Park, PA 16802, USA*

⁵*Department of Astronomy & Astrophysics, The Pennsylvania State University, University Park, PA 16802, USA*

⁶*Dipartimento di Fisica, Università di Trento, Via Sommarive 14, 38123 Trento, Italy and*

⁷*INFN-TIFPA, Trento Institute for Fundamental Physics and Applications, via Sommarive 14, I-38123 Trento, Italy*

(Dated: November 15, 2021)

We present fitting formulae for the dynamical ejecta properties and remnant disk masses from the largest to date sample of numerical relativity simulations. The considered data include some of the latest simulations with microphysical nuclear equations of state (EOS) and neutrino transport as well as other results with polytropic EOS available in the literature. Our analysis indicates that the broad features of the dynamical ejecta and disk properties can be captured by fitting expressions, that depend on mass ratio and reduced tidal parameter. The comparative analysis of literature data shows that microphysics and neutrino absorption have a significant impact on the dynamical ejecta properties. Microphysical nuclear EOS lead to average velocities smaller than polytropic EOS, while including neutrino absorption results in larger average ejecta masses and electron fractions. Hence, microphysics and neutrino transport are necessary to obtain quantitative models of the ejecta in terms of the binary parameters.

I. INTRODUCTION

The UV/optical/NIR transient AT2017gfo [1–14], counterpart of the gravitational-wave signal GW170817 [15–18], is explained as the kilonova signal from the radioactive decay of r -process elements synthesized in the mass ejected during binary neutron star mergers [10, 19–32]. Minimal models of the kilonova AT2017gfo require at least two ejecta components to account for the observed light curves: a lanthanide-poor (for the blue signal) and a lanthanide-rich (for the red signal) one [10, 28–32]. These components are often identified as the dynamical ejecta and the wind ejecta from the remnant disk, although simulations clearly indicate that this interpretation is not complete. *e.g.*, [33, 34]

Mass ejection in mergers can be triggered by different mechanisms acting on different timescales (see [35–38] for reviews on various aspects of the problem). Simulations robustly identify dynamical ejecta, of mass $M_{\text{ej}} \sim \mathcal{O}(10^{-4} - 10^{-2}) M_{\odot}$ launched during merger at average velocities $\langle v_{\infty} \rangle \sim 0.1 - 0.3 c$, *e.g.*, [23, 24, 39–45], and (for many fiducial postmerger configurations) more massive but slower winds launched on secular timescales from the remnant disk [33, 46–58]. The most accurate approach to compute the dynamical ejecta and the remnant evolution is to employ ab-initio 3+1 simulations in numerical relativity, *e.g.*, [39, 41–45, 59–68]. The increasing amount of data (both in terms of simulated binaries, physics input and numerical resolutions) allows us to explore the dependencies of ejecta and remnant properties on the binary parameters. Fitting formulae of numerical relativity data for the dynamical ejecta and remnant disk

properties from binary neutron star mergers have been previously presented in [64, 69, 70]. The interest in these formulae is at least twofold. On the one hand, they can be used to identify the main parametric dependencies of the ejecta mechanisms; on the other hand, they can be employed to constrain the source parameters from kilonova observations, *e.g.*, [31, 71–73]. Additionally, they are key to predict the amount and the properties of the ejecta that enter chemical evolution models, *e.g.*, [74].

Here we employ an extended set of data presented in previous works that includes also recent simulations with approximate neutrino transport and large mass ratios [34, 65, 68, 75].

We re-calibrate the fit models proposed in the literature with this extended dataset. Additionally we test simple polynomials as fitting models for the ejecta mass, velocity, and electron fraction.

Throughout the paper we label the two NSs with subscripts A, B . The individual gravitational masses are indicated as M_A, M_B , the baryonic masses as M_{bA}, M_{bB} , the total mass as $M = M_A + M_B$, and the mass ratio $q = M_A/M_B \geq 1$.

We define the quadrupolar tidal parameters as $\Lambda_i \equiv 2/3 C_i^{-5} k_i^{(2)}$ where $k_i^{(2)}$ is the dimensionless gravitoelectric Love number [78], $C_i \equiv GM_A/(c^2 R_A)$ the compactness parameter, and $i = A, B$. The reduced tidal parameter [79] is:

$$\tilde{\Lambda} = \frac{16 (M_A + 12M_B) M_A^4 \Lambda_A}{13 M^5} + (A \leftrightarrow B). \quad (1)$$

We use CGS units except for masses and velocities, given in units of M_{\odot} and c , respectively.

TABLE I. Datasets with the dynamical ejecta data and disk masses employed in this work. The available data is shown in the columns starting from the fourth, that contain: gravitational mass of the binary, baryonic mass of the binary, reduced tidal parameter, ejecta mass, ejecta velocity, ejecta electron fraction, disk/torus mass. EOS are either microphysical or piecewise polytropic (PWP). Neutrino schemes are: leakage, leakage + M0 or M1 for free streaming neutrinos, or M1. The compiled data are available online at [76].

Ref.	EOS	Neutrinos	M	M_b	$\tilde{\Lambda}$	M_{ej}	v_{ej}	Y_e	M_{disk}	Dataset
[65]	Micro	Leak+M0	✓	✓	✓	✓	✓	✓	✓	M0RefSet & M0/M1Set
[75]	Micro	Leak+M0	✓	✓	✓	✓	✓	✓	✓	M0RefSet & M0/M1Set
[68]	Micro	Leak+M0	✓	✓	✓	✓	✓	✓	✓	M0RefSet & M0/M1Set
[34]	Micro	Leak+M0	✓	✓	✓	✓	✓	✓	✓	M0RefSet & M0/M1Set
[45]	Micro	M1	✓	✓	✓	✓	✓	✓	✗	M0/M1Set
[42]	Micro	Leak+M1	✓	✗	✗	✓	✗	✓	✗	M0/M1Set
[44]	Micro	Leak+M1	✓	✗	✗	✓	✓	✓	✓	M0/M1Set
[64] (M0)	Micro	Leak+M0	✓	✓	✓	✓	✓	✓	✓	M0/M1Set
[63]	Micro	Leak	✓	✓	✗	✓	✓	✗	✗	LeakSet
[64] (LK)	Micro	Leak	✓	✓	✓	✓	✓	✓	✓	LeakSet
[66]	PWP	-	✓	✓	✓	✓	✗	✗	✓	NoNusSet
[77]	PWP	-	✓	✓	✓	✓	✓	✗	✓	NoNusSet
[77]	PWP	-	✓	✓	✓	✓	✓	✗	✓	NoNusSet
[59]	PWP	-	✓	✗	✗	✓	✓	✗	✗	NoNusSet
[40]	Micro	-	✓	✗	✗	✓	✓	✗	✗	NoNusSet

II. DATA AND METHOD

The datasets used in this paper are summarized in Tab. I. We group them with respect to the employed neutrino treatment:

- **M0/M1Set** comprises a set of models with neutrino emission and absorption and microphysical EOS. It includes 8 models with leakage+M0 of [64] and models of [42, 44, 45] in which a leakage+M1 scheme or a M1 gray scheme are employed for the neutrino transport. Models reported in these works span $q \in [1, 1.30]$, $\tilde{\Lambda} \in [340, 1437]$, $M_{\text{tot}} \in [2.52, 2.88]$, and $M_{\text{chirp}} \in [1.10, 1.25]$.
- **M0RefSet** harbors models with similar physical setup as those of **M0/M1Set** (specifically, they were computed with the same setup as models with leakage+M0 neutrino scheme of [64]). Presented in [34, 65, 68, 75] these models are uniform in terms of the numerical setup, code and physics and have fixed chirp mass. For that reason we group them into a separate, reference dataset. The models of this set span $q \in [1, 1.82]$, $\tilde{\Lambda} \in [400, 850]$, $M_{\text{tot}} \in [2.73, 2.88]$ with the chirp mass $M_{\text{chirp}} = 1.19$.
- **LeakSet** comprises models with leakage scheme as neutrino treatment and microphysical EOS. The dataset includes a subset of models from [64] (35 runs denoted as LK), and the set of models from [63]. The models in this dataset span $q \in [1, 1.31]$, $\tilde{\Lambda} \in [116, 1688]$, $M_{\text{tot}} \in [2.40, 3.42]$, and $M_{\text{chirp}} \in [1.04, 1.49]$.
- **NoNusSet** is composed of models with piecewise-polytropic EOSs [40, 59, 60, 66, 77], in which temperature effects are approximated by a gamma-law

pressure contribution, while composition and weak effects are neglected. The models in this dataset span $q \in [1, 2.06]$, $\tilde{\Lambda} \in [50, 3196]$, $M_{\text{tot}} \in [2.4, 4.0]$, and $M_{\text{chirp}} \in [1.04, 1.74]$.

In total we collect 324 models. For 271 of them we have/compute the binary parameters required for the analysis. For all of them the ejecta mass, M_{ej} , is available. For the models in [66] the ejecta velocity is not reported, thus only for 246 models the mass-averaged ejecta velocity, $\langle v_{\infty} \rangle$, is given. In addition to **NoNusSet** models, the average electron fraction of the ejecta is not provided also in [63]. Hence, there are 99 models for which the mass-averaged electron fraction of the dynamical ejecta, $\langle Y_e \rangle$, is available. Finally, for 76 models the root mean square (RMS) half opening angle of the outflow about the equatorial plane, $\langle \theta_{\text{RMS}} \rangle$, is available. The disk mass, M_{disk} , is provided for 119 models.

Since uncertainties estimates are not available for all datasets, we assign errors following Ref. [64], that were motivated by the observed resolution dependency of ejecta properties. Different error measures, if adopted consistently, do not change results qualitatively, as we show in the case of **M0RefSet** in Appendix C. For the dynamical ejecta mass we consider an uncertainty given by:

$$\Delta M_{\text{ej}} = 0.5 M_{\text{ej}} + 5 \times 10^{-5} M_{\odot}. \quad (2)$$

For the ejecta velocity and for the electron fraction we consider $\Delta v_{\text{ej}} = 0.02 c$ and $\Delta Y_e = 0.01$ as fiducial uncertainties, respectively. The latter value is justified by the robust behavior of the average electron fraction in simulations where multiple resolutions are available ¹.

¹ We expect larger uncertainties due to the approximate nature of

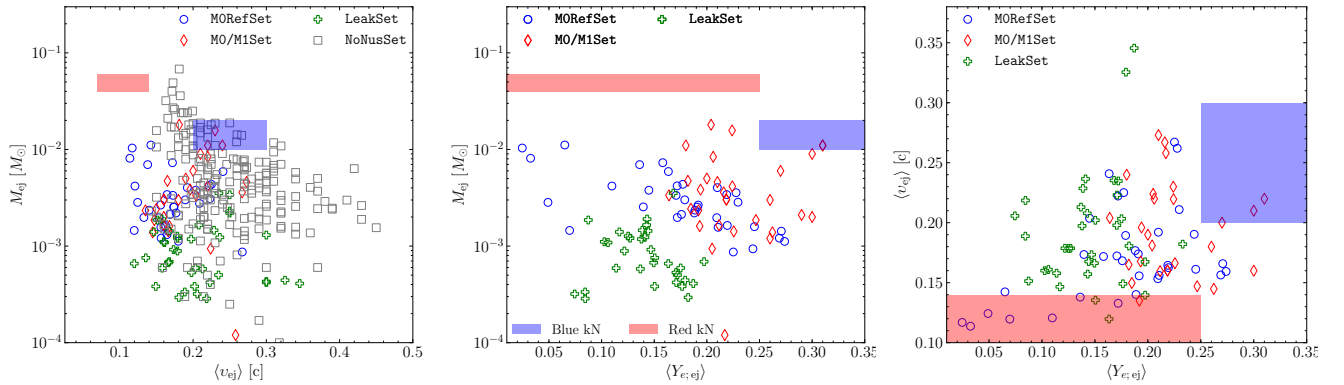


FIG. 1. Summary of dynamical ejecta properties used in this work. Blue circles represent models of **M0RefSet**, red diamonds stands for models from **M0/M1Set**, green crosses are models from **LeakSet** and gray squares stand for models from **NoNusSet**. We show for comparison the two-component fit to AT2017gfo as colored patches from [29, 80].

For the disk mass we assume [64]

$$\Delta M_{\text{disk}} = 0.5 M_{\text{disk}} + (5 \times 10^{-4}) M_{\odot}. \quad (3)$$

In this paper we aim to assess (i) the quality of the various fitting formulae to the ejecta properties and the disk mass. Because of the limited number of simulations in datasets, and having in mind multimessenger applications, instead of analyzing each dataset individually, in the main text we employ the following strategy. We study the progressively larger sample of simulations by iteratively adding datasets, starting from **M0RefSet**. The order in which we add the datasets is governed by the complexity of the physical setup, *i.e.*, **M0/M1Set**, **LeakSet** and finally **NoNusSet**. By progressively including datasets into the analysis we provide a suite of possible calibrations that can either contain the simulations with the most advanced physics input but relatively small number of them (*i.e.*, **M0RefSet** and **M0/M1Set**), or all the simulations available. Using the standard statistical methods we rank the fitting formulae and discuss their application. Additionally, we assess (ii) how the progressive inclusion changes the statistical properties of the enlarged set of simulations, aiming to assess the impact that simulating microphysics and neutrino transport has on the ejecta properties. Finally, we elaborate on which fitting formula and what calibration are favorable based on our analysis in the discussion and directly apply it to modeling the key kilonova properties.

For (i) we consider the fitting formulae that exist in the literature as well as new fitting formulae based on simple polynomials in the key BNS parameters *i.e.*, reduced tidal deformability, $\tilde{\Lambda}$, and mass ratio, q . Then we perform a standard fitting procedure with least square

method, minimizing the residuals and display the fit performance on the residual plots for every quantity. To quantitatively gauge the fit performance (for each ejecta property) we employ the sum of squared residuals (SSR) defined as $\text{SSR} = \sum_{i=1}^N (o_i - e_i)^2$ and the reduced χ^2 statistics:

$$\chi_{\nu}^2 = \frac{\chi^2}{N - C} = \frac{1}{N - C} \sum_{i=1}^N \left(\frac{o_i - e_i}{o_i^{\text{err}}} \right)^2, \quad (4)$$

where N is the number of points in the dataset, C is the number of coefficients in the fitting model (thus $N - C$ defines the number of degrees of freedom), o_i are the dataset values and o_i^{err} their errors, e_i are the values predicted by the fitting model, and $o_i - e_i$ are the residuals. The model comparison thus states that the lower SSR is and the closer to 1 χ_{ν}^2 is, the better the model performs. Note: a fit with the lowest χ_{ν}^2 may not necessarily be the fit with the lowest residuals if the error measure is not constant, *e.g.*, for M_{ej} and M_{disk} . This allows us to further assess the influence of the error measure.

This procedure is repeated for every dataset added. We provide the calibration for all fitting formulae and for all sets of datasets. We also perform the analysis for all datasets individually. Results, reported in Appendix B corroborate the ones stated in the main text.

For (ii) we employ the following procedure. We start with the set that is uniform in physics and code, the **M0RefSet** that covers a narrow range in parameter space and allows to establish the base line. Then we add the rest of the models with neutrino heating and cooling effects, the **M0/M1Set**, and assess how the basic statistical properties have changed, employing the simplest quantitative measure that characterizes a statistical ensemble, and standard deviation. To investigate the effects of the absence of neutrino reabsorption, we add the dataset that does not include this effect, the **LeakSet** and repeat the analysis. Finally, to assess the effect of the absence of

current neutrino treatments (see *e.g.*, [81, 82]). However, due to the lack of extensive comparison studies, we consider only the numerical resolution error.

neutrino cooling and differences in the EOS treatment we repeat the analysis with all datasets, including the **NoNusSet**. This iterative procedure allows to gauge the qualitative effect that different physical treatments have of the statistical behavior of the ejecta parameters and disk mass. We leave a more rigorous quantitative analysis to future works, when larger sample of data with physically motivated error measures and that cover a broader range in parameter space becomes available.

III. DYNAMICAL EJECTA

The mechanism behind the production of dynamical ejecta as well as the details on the numerical relativity simulations of **M0RefSet** are discussed in *e.g.*, [34, 37, 38]. Here, we focus on overall properties of the mass ejecta in relation to other results in the literature, and provide approximate fitting formulae for the total ejecta mass, the mass-averaged velocity, the electron fraction and the RMS half opening angle. Importantly, there are several criteria for a fluid element to become gravitationally unbound – to become ejecta. Due to the “burst-like” nature of dynamical ejecta, the geodesic criterion, that considers fluid elements moving on ballistic trajectories, neglecting the fluid pressure [83], is commonly employed [43, 64, 68]. Another broadly used criterion is the Bernoulli criterion, that takes into account the internal energy of the fluid. With respect to the dynamical ejecta, these two criteria were found to lead to the ejecta mass estimations different by a factor of 2 [84]. Additionally, depending on the length of the postmerger evolution of a simulation, different methods are employed to compute the ejecta properties. For instance, in [64], the ejecta was computed following the matter passing an extraction sphere until the matter flux subsided. Simulations were sufficiently long to allow the mass flux to saturate. Meanwhile in [45], a combination ejecta that was able to leave the simulation domain and that was still within the domain of the simulation at the end was considered. These differences in ejecta criteria and method of calculation present an additional source of systematics in data.

Figure 1 summarizes the total mass, the mass-averaged velocity and mass-averaged electron fraction (where available) for the used datasets. Overall we note that the ejecta properties of the models of **M0RefSet** are compatible with those of **M0/M1Set**, as they include the same physics with respect to the EOS treatment and also include the effect of neutrino absorption. Notably, the very high mass-ratio, q , models of **M0RefSet**, discussed in [68], show slightly different properties, as their ejecta is of tidal origin only. Comparing the properties of **M0/M1Set** and **LeakSet** we observe that neutrino absorption leads, on average, to a larger ejecta mass, which is especially noticeable for the leakage subset of [64](LK). Additionally, neutrino absorption leads to a higher $\langle Y_e \rangle$ of the ejecta, while the average velocity, $\langle v_\infty \rangle$, appears to be independent of it.

In the following we discuss the fitting formulae for the different quantities.

A. Mass

In order to assess the systematic changes in ejecta masses between different datasets with different physics input, we restrict the binary parameter space to $q \in (1, 1.2)$ and $\tilde{\Lambda} \in (350, 850)$, common for all datasets that we compare. In doing so we reduce the number of simulations significantly. Thus, we aim to assess the changes on the qualitative level only. A more rigorous analysis would require significantly larger sample of simulations, homogeneously distributed in the parameter space. The dynamical ejecta mass, averaged over 8 simulations of **M0RefSet** is $\bar{M}_{\text{ej}} = (3.5 \pm 1.3) \times 10^{-3} M_\odot$ where hereafter we report also the standard deviation computed over the relevant simulation sample².

Adding the rest of **M0/M1Set** (7 models) we obtain $(5.1 \pm 3.9) \times 10^{-3} M_\odot$. The increase is given largely by datasets that include the M1 neutrino scheme, [45] and [44]. However, adding models of **LeakSet**, (another 8 models) we observe that the mean value decreases to $3.8 \times 10^{-3} M_\odot$, as models without neutrino absorption predict, on average, lower ejecta masses. Finally, adding models without neutrinos at all, some of which have polytropic EOS (7 models in the restricted parameter space), we do not observe change in the \bar{M}_{ej} .

Lifting the restrictions on the parameter space, we fit all the available data using second-order polynomials in one parameter ($\tilde{\Lambda}$), and in two parameters, $(q, \tilde{\Lambda})$, namely:

$$P_2^1(\tilde{\Lambda}) = b_0 + b_1 \tilde{\Lambda} + b_2 \tilde{\Lambda}^2, \quad (5)$$

$$P_2^2(q, \tilde{\Lambda}) = b_0 + b_1 q + b_2 \tilde{\Lambda} + b_3 q^2 + b_4 q \tilde{\Lambda} + b_5 \tilde{\Lambda}^2. \quad (6)$$

Additionally, we consider the fitting model presented Refs. [64, 69, 85]

$$\left(\frac{M_{\text{ej}}}{10^{-3} M_\odot} \right)_{\text{fit}} = \left[\alpha \left(\frac{M_B}{M_A} \right)^{1/3} \left(\frac{1 - 2C_A}{C_A} \right) + \beta \left(\frac{M_B}{M_A} \right)^n + \gamma \left(1 - \frac{M_A}{M_{bA}} \right) \right] M_{bA} + (A \leftrightarrow B) + \delta, \quad (7)$$

and the model presented in [70]:

$$\left(\frac{M_{\text{ej}}}{10^{-3} M_\odot} \right)_{\text{fit}} = \left(\frac{\alpha}{C_A} + \beta \frac{M_B^n}{M_A^n} + \gamma C_A \right) M_A + (A \leftrightarrow B). \quad (8)$$

² We report here the mean value as it is the simplest quantitative measure to characterize the differences between the different datasets.

TABLE II. Values of SSR for different fitting models for the dynamical ejecta properties. Mean is the simulation average, $P_n(x, y)$ is a polynomial of order n in the variables x, y . Fits are performed for the data of this work and for an increasingly larger combined dataset from the literature. See text for discussion. The best fitting model for a given dataset is characterized by the lowest value of SSR.

$\log_{10}(M_{\text{ej}})$	Datasets	Mean	Eq. (7)	Eq. (8)	$P_2^1(\tilde{\Lambda})$	$P_2^2(q, \tilde{\Lambda})$
	MORefSet	2.57	1.65	1.40	2.43	0.97
	& M0/M1Set	8.19	7.51	6.35	7.84	6.55
	& LeakSet	33.13	26.37	21.57	29.62	24.40
	& NoNusSet	86.93	80.08	63.38	86.85	55.09
$\langle v_{\text{ej}} \rangle$	Datasets	Mean	Eq. (9)	$P_2^1(\tilde{\Lambda})$	$P_2^2(q, \tilde{\Lambda})$	
	MORefSet	0.04	0.02	0.04	0.01	
	& M0/M1Set	0.09	0.05	0.07	0.04	
	& LeakSet	0.29	0.24	0.25	0.21	
	& NoNusSet	0.78	0.66	0.74	0.67	
$\langle Y_e \rangle$	datasets	Mean	$P_2^1(\tilde{\Lambda})$	$P_2^2(q, \tilde{\Lambda})$		
	MORefSet	0.14	0.13	0.02		
	& M0/M1Set	0.24	0.23	0.06		
	& LeakSet	0.35	0.35	0.23		
$\langle \theta_{\text{RMS}} \rangle$	datasets	Mean	$P_2^1(\tilde{\Lambda})$	$P_2^2(q, \tilde{\Lambda})$		
	MORefSet	2775	2631	498		
	& M0/M1Set	2949	2788	574		
	& LeakSet	4681	4116	2382		

As in some cases the values of M_{ej} change by orders of magnitude for very close values of q and $\tilde{\Lambda}$, we calibrate the fitting models to $\log_{10}(M_{\text{ej}})$ instead of the M_{ej} .

Regarding Eq. (7) and Eq. (8), we also note that these formulae deliver ill-conditioned fits, with coefficients that change up to a factor of two for the same data, depending on the guesses or on the nonlinear fitting algorithm employed. While such formulae may allow to account for a non-smooth behavior in data, their calibration presents an additional challenge.

Fitting coefficients as well as values of χ_ν^2 are reported in Appendix A: coefficients of the polynomial regressions are reported in Tab. IV; fits coefficients for Eqs.(7)-(8) are reported in Tab. V.

Different fits for the dynamical ejecta properties are compared in terms of the sum of squared residuals, SSR, in Tab. II. We find that fitting the data from only MORefSet as well as all the data from all datasets combined, the lowest SSR is given by $P_2^2(q, \tilde{\Lambda})$. The Eq. (8) gives similar, albeit slightly larger values for these sets of simulations, while performing slightly better for the other two combinations of datasets. Invoking the error measure and the χ_ν^2 statistic we observe a very similar picture with $P_2^2(q, \tilde{\Lambda})$ giving the lowest χ_ν^2 when all datasets are considered and Eq. (8) performing better when only M0/M1Set and MORefSet are considered. The small difference in performance between these two fitting formulae can be attributed to the fact that both include the mass ratio explicitly, which allows to capture the leading trend in the data.

The Eq. (7) cannot sufficiently well reproduce the low ejecta masses of models with microphysic EOS and leakage neutrino transport scheme and high ejecta masses

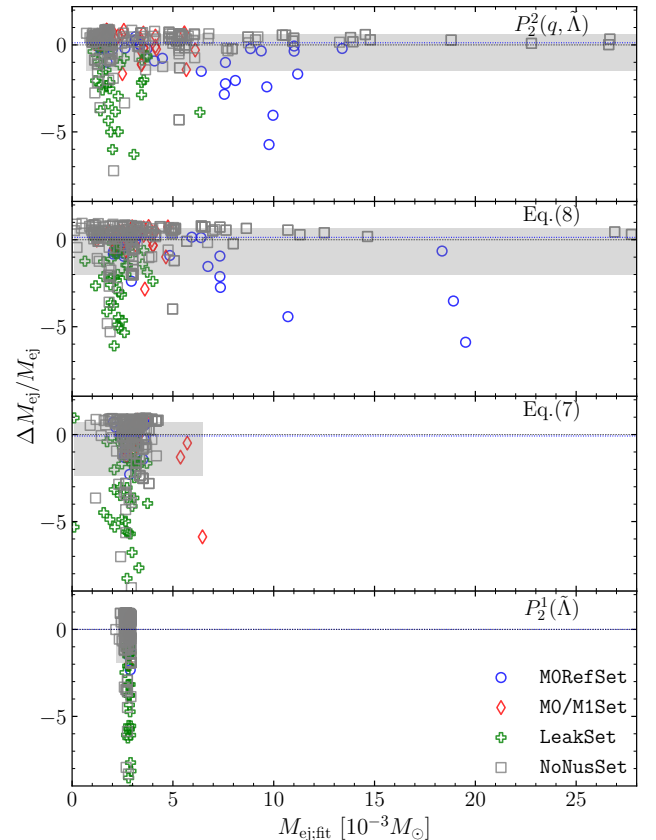


FIG. 2. Relative differences between data and fits for the dynamical ejecta mass, $\Delta M_{\text{ej}} = M_{\text{ej}} - M_{\text{ej}}^{\text{fit}}$. We show polynomial fits and fitting formulae Eq. (7) and Eq. (8) calibrated with all datasets available. From top to bottom the models arrange based on their SSR: from lowest to highest See Tab. II. The gray region represents the fit's 68% confidence level. Note that fitting was performed minimizing $\log_{10}(M_{\text{ej}})$. See text for details.

of models with polytropic EOS and no neutrino transport. This results in the truncated $M_{\text{ej,fit}}$ (see Fig. 2) and larger SSR and χ_ν^2 . In addition, it was previously found in [64], that this fit model does not accurately reproduce the data and misses systematic trends. The simplest model, a polynomial of only $\tilde{\Lambda}$, cannot capture leading trends in the data, resulting in considerably larger SSR and χ_ν^2 once all datasets are considered. Similarly, taking the simple mean value as a fitting model results in an even larger SSR and χ_ν^2 . Thus, the inclusion of the dependency on mass-ratio is of crucial importance for modeling dynamical ejecta mass.

In Fig. 2 we show the relative differences between all datasets values and values from the fitting models. We observe that none of the fitting models can adequately capture the subset of LeakSet with a leakage scheme only as neutrino treatment, (Cf. [63, 64]). While the lowest SSR and χ_ν^2 are found for $P_2^2(q, \tilde{\Lambda})$, the plot shows that the Eq. (8) can also capture the large ejecta mass of

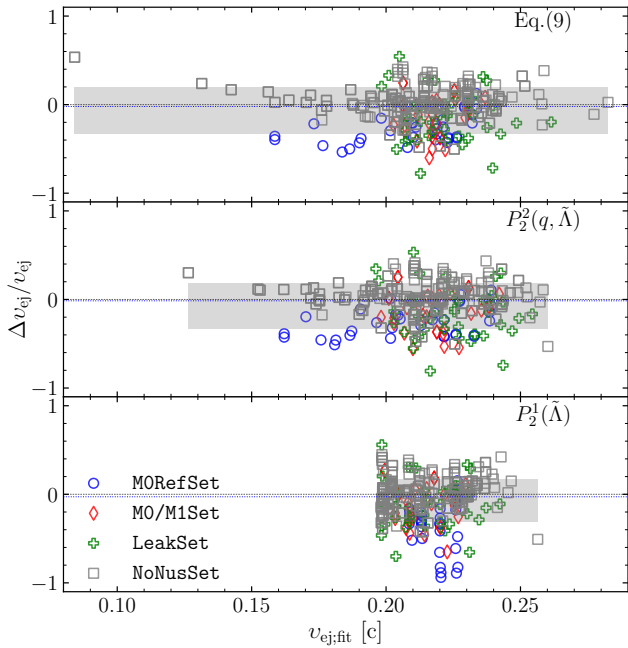


FIG. 3. Relative differences between data and fits for the mass-averaged velocity of the dynamical ejecta, $\Delta v_{\text{ej}} = v_{\text{ej}} - v_{\text{ej}}^{\text{fit}}$. Calibration is done for all datasets available. We show the fitting formula Eq. (9) and the polynomial fits. From top to bottom the models are arranged based on their χ_{ν}^2 : from lowest to highest.

NoNusSet and M0RefSet with however higher residuals. Notably Eq. (7) cannot capture that tail, truncating the distribution at $\sim 10^{-2} M_{\odot}$. The polynomial in $\tilde{\Lambda}$ fits the data very poorly, showing an almost flat distribution around the mean value of the ejecta mass.

B. Mass-averaged velocity

The mass-averaged terminal velocity of the dynamical ejecta, $\langle v_{\infty} \rangle$, from M0RefSet ranges from $0.11c$ to $0.27c$, in agreement with the leakage simulations performed with the same code in [64]. However, differently from the analysis of [64], the correlation of the $\langle v_{\infty} \rangle$ with the tidal parameter $\tilde{\Lambda}$ was found in the models of M0RefSet with the fixed chirp mass [34]. Models with lower $\tilde{\Lambda}$, showed higher velocities. This is a consequence of the fact that the dynamical ejecta in comparable-mass mergers are dominated by the shocked component and that the shock velocity is larger the more compact the binary is. On the contrary, for high mass ratios $q \gtrsim 1.5$, the ejecta are dominated by the tidal component and a larger q leads to a smaller $\langle v_{\infty} \rangle$ in M0RefSet.

Restricting the parameter space again, we assess the change in mean value of ejecta velocity, $\langle v_{\infty} \rangle$. For the models of M0RefSet we find $\overline{\langle v_{\infty} \rangle} = 0.19 \pm 0.03c$. When we iteratively add models of M0/M1Set, LeakSet and

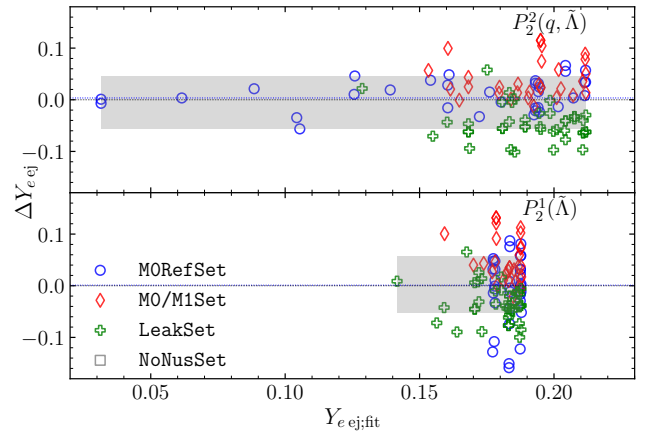


FIG. 4. Relative differences between data and fits for the mass-averaged electron fraction of the dynamical ejecta. We show the polynomial fits, and Eq. (5) and Eq. (6). Calibration is done for all datasets available. Here $\Delta Y_{e,\text{ej}} = Y_{e,\text{ej}} - Y_{e,\text{ej}}^{\text{fit}}$. From top to bottom the models are arranged based on their χ_{ν}^2 : from lowest to highest.

NoNusSet, the $\overline{\langle v_{\infty} \rangle}$ remains largely unchanged, taking values of $0.20c$, $0.20c$ and $0.21c$. Notably, Fig. 1, shows that some models of NoNusSet (models of Cf. [40]³) have an overall larger velocity. However, they lie outside of the restricted parameter space.

Lifting the restrictions on the parameter space we fit the data with a second-order polynomials, as in Eq. (5), and also with the fit formula reported in [64, 77]:

$$\langle v_{\infty} \rangle_{\text{fit}} = \left[\alpha \left(\frac{M_A}{M_B} \right) (1 + \gamma C_A) \right] + (A \leftrightarrow B) + \beta. \quad (9)$$

We note, that similarly to the Eq. (7) and Eq. (8), the outcome of the calibration of the Eq. (9) depends on the initial guesses of the minimization algorithm.

The coefficients of the polynomial regressions for $\langle v_{\infty} \rangle$ are reported in Tab. IV; fits coefficients for Eq. (9) are reported in Tab. V. The fit models' performance is summarized in Tab. II in terms of SSR.

We find that unless models of NoNusSet are included, the $P_2^2(q, \tilde{\Lambda})$ displays the lowest SSR and χ_{ν}^2 among other fitting formulae. When models of NoNusSet are also included, the $P_2^2(q, \tilde{\Lambda})$ and Eq. (9) perform rather similar.

In Fig. 3 we show the differences between the data and the fits for the considered fitting models. We find that Eq. (9) and the second order polynomial in $(q, \tilde{\Lambda})$ reproduce most of the data within an error of $\sim 50\%$ and overall perform very similarly. In both cases, the largest deviations are obtained for models of the LeakSet, with the neutrino leakage scheme. The one parameter polynomial of $\tilde{\Lambda}$ fails to capture the low velocity tail of the

³ In [40] the different treatment of gravity was employed. Specifically, the evolution was performed under the assumption of conformal flatness.

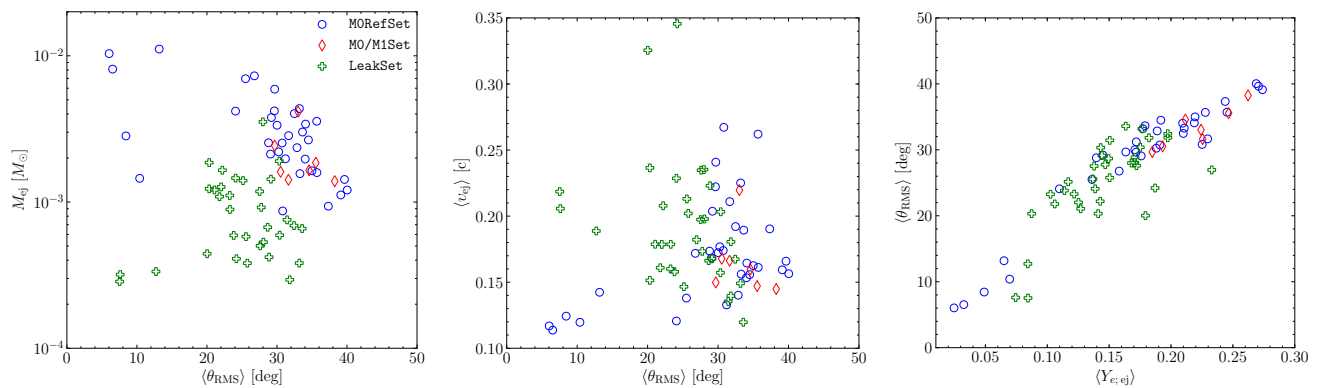


FIG. 5. Relations between the ejecta θ_{RMS} and other parameters of the dynamical ejecta: mass, M_{ej} , velocity, $\langle v_{\infty} \rangle$, and electron fraction $\langle Y_e \rangle$ for models from **M0RefSet** and [64] from **LeakSet** and **M0/M1Set**. Plots show that models with neutrino absorption have higher M_{ej} and larger θ_{RMS} as well as a clear correlation between θ_{RMS} and $\langle Y_e \rangle$.

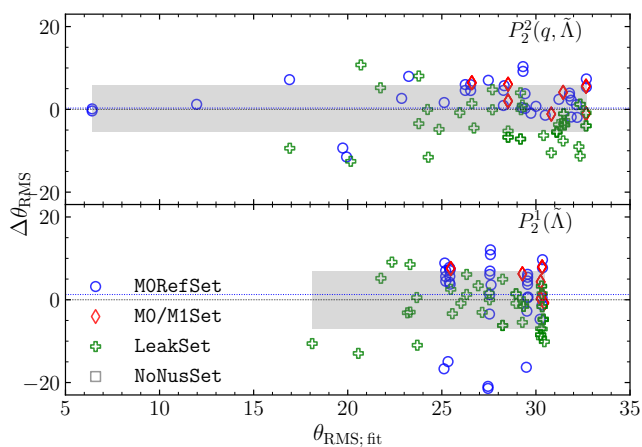


FIG. 6. Relative differences between data and fits of dynamical ejecta mass-averaged electron fraction. We show polynomial fits only. Here $\Delta\theta_{\text{RMS}} = \theta_{\text{RMS}} - \theta_{\text{RMS}}^{\text{fit}}$. From top to bottom the models are arranged based on their χ_{ν}^2 : from lowest to highest.

distribution and overall gives considerably higher differences between the dataset and the model predicted values of $\langle v_{\infty} \rangle$.

C. Electron fraction

The mass-averaged electron fraction, $\langle Y_e \rangle$, in **M0RefSet** varies from 0.03 to 0.27.

Restricting the parameter space to the common region, we obtain the mean value of electron fraction for **M0RefSet** $\langle Y_e \rangle = 0.19 \pm 0.02$. Adding models of **M0/M1Set** increases the mean to 0.20 ± 0.04 which is largely due to models of [42, 44] with leakage+M1 scheme (see Fig. 1). When models of the **LeakSet** are added, the mean values decreases back, which is as expected as models with leakage scheme only have lower ejecta electron fraction

e.g., [64]. Notably, the number of simulations added is rather small⁴.

Regarding the fitting functions, we explore the low-order polynomials in $(q, \tilde{\Lambda})$ and in $(\tilde{\Lambda})$ only. The coefficients of polynomial regressions are reported in Tab. IV. We observe that for all datasets, the $P_2^2(q, \tilde{\Lambda})$ displays consistently lower SSR and χ_{ν}^2 . Notably, the addition of **LeakSet** models leads to a jump in these measures, as the data in this set is statistically different (different physics setup). In Fig. 4 we show the performance of the different fitting models for the mass-averaged electron fraction of the ejecta. When all datasets are considered, the second order polynomial manages to reproduce both the low- Y_e tail and high Y_e values for models with advanced neutrino treatment. The accurate computation of the electron fraction naturally requires neutrino absorption to be included into simulation setups. The availability of a larger number of simulations with advanced neutrino transport will undoubtedly improve fitting models.

D. Root mean square half opening angle

Ejecta geometry was found to have a strong imprint on the properties of the electromagnetic counterparts to mergers [*e.g.*, 31]. Numerical relativity simulations show that the form of the angular distribution of ejecta properties is quite complex [*e.g.*, 64] and presents challenges for a statistical analysis. Here we employ the mass-averaged RMS half opening angle (under the assumption of axial symmetry), a quantity that can be used to separate the massive, low-latitude outflow and less massive, polar one. In the Discussion we show an example of how this quantity can be used in kilonova modeling. Following [64], we define the mass-averaged RMS half opening angle as by

⁴ Note that [63] does not provide electron fraction.

assuming axial symmetry and computing:

$$\theta_{\text{RMS}} = \frac{180}{\pi} \left(\frac{\sum m_i \theta_i^2}{\sum m_i} \right)^{1/2}, \quad (10)$$

where θ_i and m_i are the angle (from the binary plane) and mass of the ejecta element. This quantity is available only for **MORefSet** and for the models of [64]. In Figure 5 we show the dependency of θ_{RMS} on the previously discussed ejecta parameters. Comparing the data from **MORefSet** and the leakage dataset of Ref. [64], we find that the inclusion of neutrino absorption leads to larger θ_{RMS} on average with the exception of highly asymmetric models of **MORefSet**. Notably we observe a clear linear relation between the θ_{RMS} and $\langle Y_e \rangle$ (see Fig. 5). The origin of this relation lies in the dependency of the ejecta properties on the binary mass-ratio. Asymmetric binaries produce low- Y_e , tidal ejecta confined largely to the lane of the binary, while for more symmetric models with prominent shocked ejecta component there is a trend to have higher Y_e and more spread-out ejecta. This further suggests that θ_{RMS} can help capturing the transition between the low- and high-opacity ejecta in kilonova modeling.

The number of models within the restricted parameter space for which we have the θ_{RMS} is very limited. Thus we only report the average value for **MORefSet**, $\langle \theta_{\text{RMS}} \rangle = (31.7 \pm 1.9)$ deg.

In light of the considerably smaller sample of models for which we have θ_{RMS} , we simplify the statistical analysis, considering as fitting models only polynomials: $P_2^1(\tilde{\Lambda})$ and $P_2^2(q, \tilde{\Lambda})$. The coefficients of the polynomial regressions are reported in Tab. IV. Following [64] we adopt a uniform error for all models of 2 degrees. We find that similarly to the case of ejecta electron fraction, the $P_2^2(q, \tilde{\Lambda})$ performs consistently better here than other options for all datasets in terms of both SSR and χ_ν^2 .

In Fig. 6 we show the performance of polynomial fitting models to the ejecta θ_{RMS} . The second order polynomial provides a better fit to the low- θ_{RMS} tail of the distribution than $P_2^1(\tilde{\Lambda})$. and reproduces the data within ~ 10 deg. Overall, we observe that the inclusion of both q and $\tilde{\Lambda}$ in a fitting formula is important for capturing the trends in data. However, the small sample of models does not allow us to conduct a more thorough investigation, in particular, to study the effects of various physics included in simulations.

E. Application of the polynomial fit

Overall, comparing the performance of different fitting formulae to the ejecta properties, we find that the $P_2^2(q, \tilde{\Lambda})$ gives a comparatively better fit when all simulation data from all datasets are considered. When only the **MORefSet** and **MO/M1Set** are considered, however, the ejecta mass is slightly better fitted by non-polynomial fitting formula, Eq. (8). The implicit inclusion of mass-ratio allows the $P_2^2(q, \tilde{\Lambda})$ to capture leading

TABLE III. Sum of squared residuals for different fit models for the final disk mass, $\log_{10}(M_{\text{disk}})$.

datasets	Mean	Eq. (11)	Eq. (12)	$P_2^1(\tilde{\Lambda})$	$P_2^2(q, \tilde{\Lambda})$
MORefSet	15.11	13.28	9.96	13.95	8.81
& MO/M1Set	17.03	14.42	11.58	15.24	10.70
& LeakSet	54.02	32.56	17.65	29.72	19.56
& NoNusSet	80.47	45.71	30.06	44.04	26.73

trends in the behaviour of $\langle v_\infty \rangle$, $\langle Y_e \rangle$ and θ_{RMS} . For its calibration we suggest datasets with the most advanced physics i.e., **MO/M1Set** and **MORefSet**. A caution must be exercised when using datasets computed with different physics input and at various resolutions, as in certain cases (e.g., M_{ej}), the systematics introduced by these differences might obscure the leading trends in data. This conclusion is supported by the analysis of the statistical behaviour of data from different datasets and further corroborated by the analysis of the individual datasets (see Appendix B). In addition to the quantitative and qualitative assessments of the fit performance via SSR, χ_ν^2 -statistics and residual plots, we consider a direct application of the, $P_2^2(q, \tilde{\Lambda})$ and compare it to the data used for calibration in Fig. 7. The plot shows that the behaviour of the fitting formula depends sensibly on the choice of datasets used for calibration, and the predictive power of the fit reduces when datasets with different physics (the difference in contour shapes between left and right column of subplots) and numerical setups are employed. The ejecta properties, especially, mass, velocity and electron fraction depend strongly on the neutrino treatment scheme and larger number of high resolution NR simulations with advanced treatment of neutrino emission and absorption is required to further constrain the statistics of ejecta properties.

IV. REMNANT DISK

The disk mass at the end of the simulation of models of **MORefSet** varies from $0.01M_\odot$ to $0.3M_\odot$. Within the restricted parameter space the mean value of the disk mass, $\overline{M}_{\text{disk}}$, for models of the **MORefSet** is $(0.12 \pm 0.05)M_\odot$ and it decreases only slightly when models from **MO/M1Set**, **LeakSet** are added, to $(0.11 \pm 0.04)M_\odot$. Notably, large variations in the mean value are observed when the parameter space is enlarged to include very asymmetric and promptly collapsing models. However, there is not enough models for the comparison. While this might suggest that the disk mass depends weakly on the physical setup of simulations, the large uncertainties in data and the fundamental difference between the disk around a neutron star and a black hole must be taken into consideration. In particular, we stress that the disk mass is estimated in different ways in the different datasets. In [60, 77] the disk is estimated only for BNS forming BH, at approximately ≈ 1 ms after collapse and computing

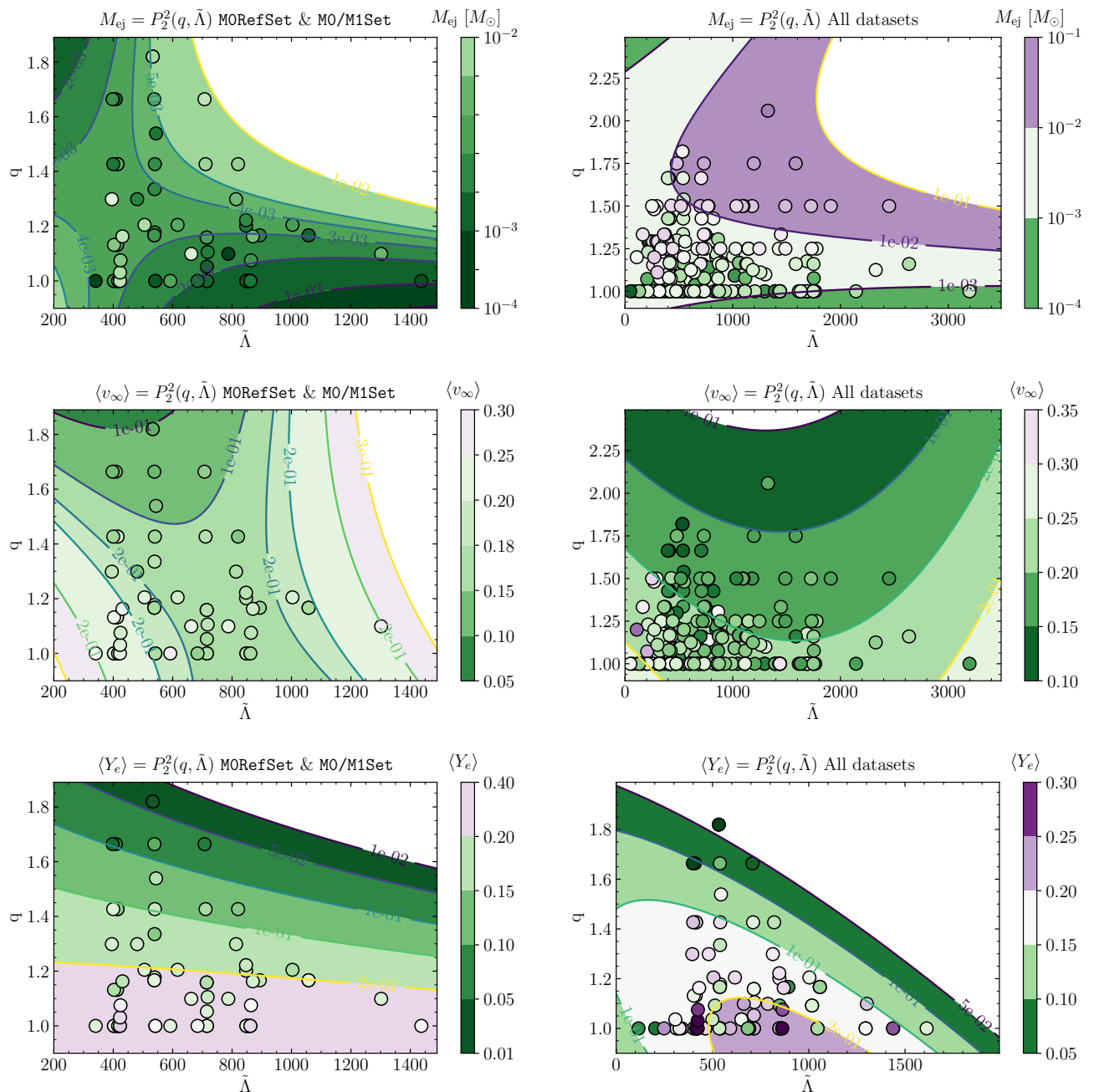


FIG. 7. Comparison between ejecta parameters informed by the fit (colored contours), and the simulation ejecta data (colored markers) for $P_2^2(q, \tilde{\Lambda})$ fitting model calibrated with advanced-physics datasets, M0RefSet and M0/M1Set, (*left column of panels*) and with all available datasets (*right column of panels*). The plot shows that for some physical quantities, such as ejecta electron fraction and velocity, the leading trends in data appear to be captured by the $P_2^2(q, \tilde{\Lambda})$ calibrated with datasets with advanced physics. When all datasets are considered, however, the limitations of the smooth polynomial fitting function becomes apparent as it is not able to fit the non-smooth data well.

the rest mass outside the apparent horizon (AH). In [44], the disk mass is extracted at ≈ 30 ms outside the AH. In [64], the disk mass is computed as the baryonic mass outside the AH at BH formation, while for NS remnants the criterion $\rho < 10^{13}$ g cm $^{-3}$ is used. In [66] for both BH and NS outcome the $\rho < 10^{13}$ g cm $^{-3}$ criterion is

used and time of the extraction is not specified. In [45] the density criterion is the same, however the simulations are significantly shorter (~ 7.5 ms) than in other works. Overall, we estimate that these differences can amount to a systematic factor of a few.

As fitting formulae we consider the polynomials Eqs (5)

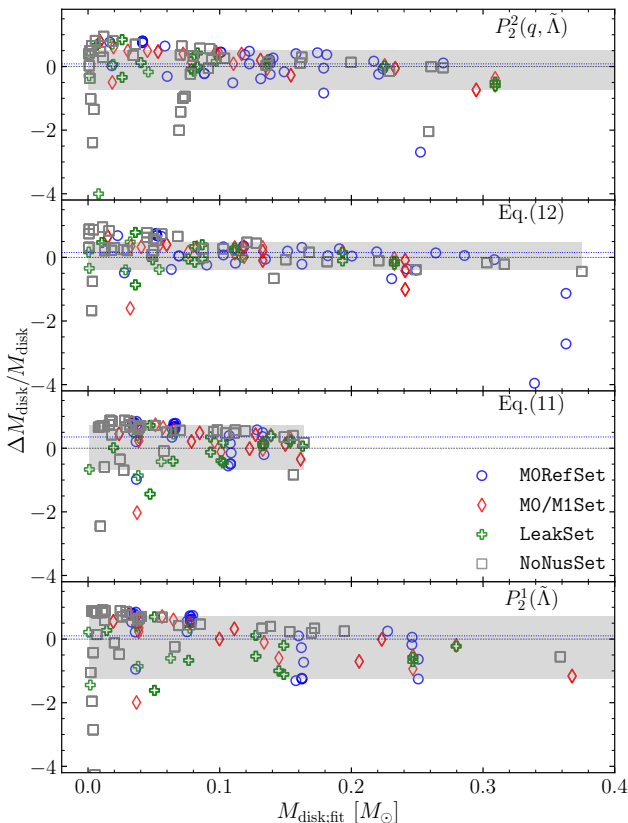


FIG. 8. Relative differences between data and the fits of the disk mass. The calibration was performed for $\log_{10}(M_{\text{disk}})$ using simulations from all datasets. Different panels show polynomial fits in $\tilde{\Lambda}$ and $(q, \tilde{\Lambda})$, fitting formulae Eq. (7) and Eq. (8). The best fitting model is characterized by the lowest value of χ_{ν}^2 . Best fitting coefficients are given in the tables in Appendix A. Here $\Delta M_{\text{disk}} = M_{\text{disk}} - M_{\text{disk}}^{\text{fit}}$. The fitting procedure here was based in minimizing residuals instead of χ_{ν}^2 as otherwise, the error measure adapted, Eq. (3), would lead to the fit underestimating most of datasets used.

and (6), and the formula provided in [64]:

Similarly to the mass of dynamical ejecta, the disk mass varies by up to an order of magnitude for, in some cases, very similar values of q and $\tilde{\Lambda}$. In order to simplify the fitting procedure and reproduce both, high and low mass tails, we consider the $\log_{10}(M_{\text{disk}})$. Notably, the Eqs. (11)-(12) are segmented, and include constant parts. For clarity we write the equations in the form used for fitting, that read

$$\begin{aligned} & \log_{10} \left(\frac{M_{\text{disk}}}{M_{\odot}} \right)_{\text{fit}} \\ &= \max \left\{ -3.0, \log_{10} \left(\alpha + \beta \tanh \left(\frac{\tilde{\Lambda} - \gamma}{\delta} \right) \right) \right\}, \end{aligned} \quad (11)$$

and the fitting formula provided in [70]:

$$\begin{aligned} & \log_{10} \left(\frac{M_{\text{disk}}}{M_{\odot}} \right)_{\text{fit}} \\ &= \log_{10}(M_A) + \max \left\{ -3.30, \log_{10} \left((\alpha C_A + \beta)^{\gamma} \right) \right\}. \end{aligned} \quad (12)$$

The exact form of polynomials, $P_2^1(\tilde{\Lambda})$ and $P_2^2(q, \tilde{\Lambda})$, used in this section then reads,

$$\begin{aligned} \log_{10} \left(P_2^1(\tilde{\Lambda}) \right) &= \log_{10} \left(b_0 + b_1 \tilde{\Lambda} + b_2 \tilde{\Lambda}^2 \right), \\ \log_{10} \left(P_2^2(q, \tilde{\Lambda}) \right) &= \log_{10} \left(b_0 + b_1 q + b_2 \tilde{\Lambda} + b_3 q^2 \right. \\ & \quad \left. + b_4 q \tilde{\Lambda} + b_5 \tilde{\Lambda}^2 \right). \end{aligned}$$

As before we opt here for the minimization of residuals in the fitting procedure. We rank the fitting formulae performance based on the SSR, augmenting the discussion with χ_{ν}^2 , computed using the error measure (3).

The coefficients of the polynomial regressions are reported in Tab. VI; the fit coefficients for Eq. (11) and Eq. (12) are reported in Tab. VII. The SSR for these fits are reported in Tab. IV. As for those for the dynamical ejecta, the formulae in Eq. (11) and Eq. (12) give ill-conditioned fits. Notably, we find that depending on the initial guess for coefficients the Eq. (12) may develop singularities when data from all datasets is fitted and no limitations are imposed upon the coefficients. However, such non-smooth fitting functions may allow to capture the complex behavior in data, not reproduced by $P_2^1(\tilde{\Lambda})$ and $P_2^2(q, \tilde{\Lambda})$

Fitting the data of M0RefSet and combined M0RefSet dataset and M0/M1Set we observe that the $P_2^2(q, \tilde{\Lambda})$ consistently shows the lowest SSR and χ_{ν}^2 . Notably, the Eq. (12) gives only slightly higher values in both cases. When all models from all datasets are considered, we again observe that the $P_2^2(q, \tilde{\Lambda})$ is statistically preferred with Eq. (12) being the close second. The observed similarity in fitting formulae performance further suggests that indeed mass-ratio and $\tilde{\Lambda}$ allow to capture the main trends in the disk mass data.

When performing the calibration of Eq. (12) and Eq. (11) with standard least-square method we observed that the result of the calibration depends strongly on the initial guesses for the coefficients. This behavior makes the use of these fitting formulae difficult from the point of view of the reproducibility of result. We also note that Eqs. (11)-(12) include constant “floor values”. The physical motivation behind these constants is not very clear and while they might help to constrain the fit behaviour at known limits of the parameter space, *e.g.*, at $\tilde{\Lambda} \rightarrow 0$, their applicability for all datasets may not be optimal. The $P_2^2(q, \tilde{\Lambda})$ fitting formula is free from aforementioned issues and allows for stable and reproducible fits.

In Fig. 8 we show the relative differences between the data and the values given by the fitting models. Here the

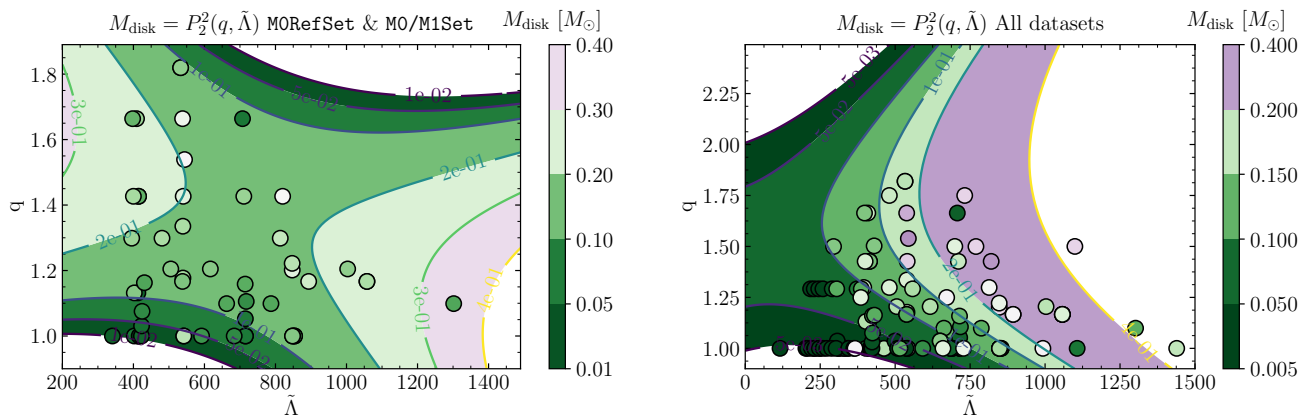


FIG. 9. Same as Fig. 7 but for the disk mass. The plot shows that at low values of q and $\tilde{\Lambda}$ the fit is able to capture the leading trends in data. However, in the region where there are fewer data present, at high q and $\tilde{\Lambda}$, the fit becomes increasingly less accurate (see text).

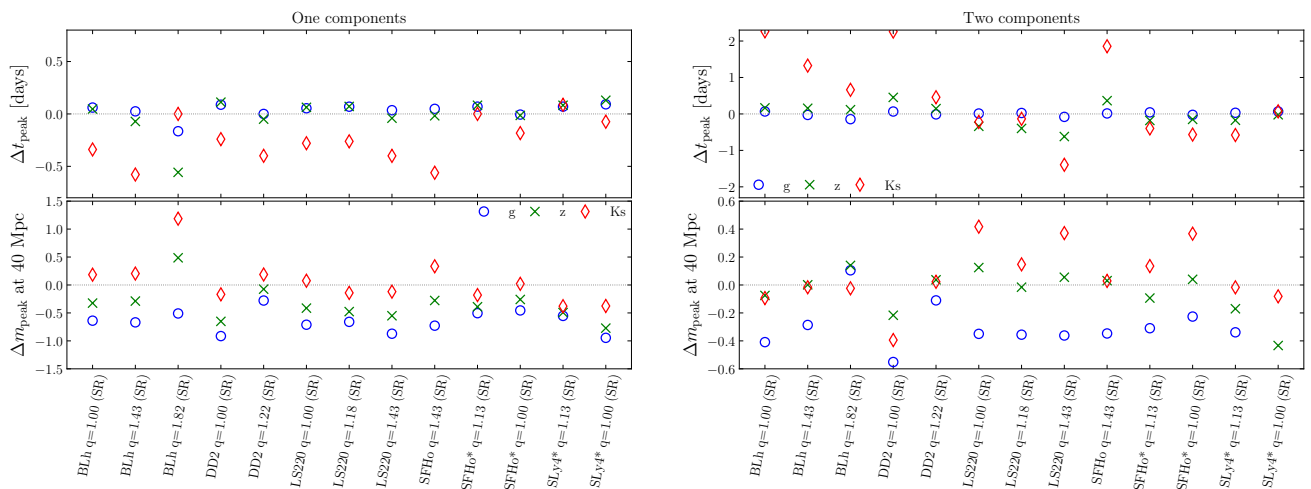


FIG. 10. Comparison between one component light curves (*left panel*) and two components light curves (*right panel*) in g , z and K_s bands using direct NR input or the fitting formulae for the dynamical ejecta and disk mass. The y -axis displays the difference between the peak time (*top panel*), $\Delta t_{\text{peak}} = t_{\text{peak;NR}} - t_{\text{peak;fit}}$, and peak magnitude, $\Delta m_{\text{peak}} = m_{\text{peak;NR}} - m_{\text{peak;fit}}$, (*bottom panel*); the x -axis shows selected BNS models of M0RefSet. The fits employed here are the polynomials in $(q, \tilde{\Lambda})$ used with the best fitting coefficients, calibrated to M0/M1Set (that includes M0RefSet). The plot shows that the light curves generated with the dynamical ejecta fits (one component) tend to underestimate the peak times and magnitudes of NR-informed light curves, especially in the K_s band. In case of dynamical ejecta and disk wind (two components) light curves, the peak time is less constrained (± 2 days) in the K_s band, but the peak magnitudes is predicted more accurately ± 0.5 mag.

relative performance of the fits can be inferred from the 67% confidence level bar. We observe that the Eq. (11) cannot reproduce the high disk masses found in asymmetric binaries of M0RefSet. Meanwhile other fitting formulae can reproduce both the low and the large disk masses with varying degree of success. Notably, the fit with Eq (12) displays the smallest residuals, *i.e.*, with the narrowest 67% confidence level bar. The second best fit here is $P_2^2(q, \tilde{\Lambda})$. The reason why the χ^2_ν for the Eq. (12) is larger than that for $P_2^2(q, \tilde{\Lambda})$ (see Tab. IV) lies in the error measure, Eq. (3), that is used only in χ^2_ν calculation. Thus, while the fit with lowest χ^2_ν provides a better fit

for lower disk masses (with tighter errors), the Eq. (12) gives a fit with overall smaller residuals.

We show the performance of the $P_2^2(q, \tilde{\Lambda})$ fitting formula in the q - $\tilde{\Lambda}$ space in Fig. 9. The plot shows that certain main trends in data, *e.g.*, higher disk mass in low- q , low- $\tilde{\Lambda}$ simulations, are reproduced by the fit calibrated with either combined M0RefSet and M0/M1Set or all datasets. However, being a smooth function, the $P_2^2(q, \tilde{\Lambda})$, cannot capture the rapid oscillations in data.

Overall, the statistical analysis shows that the value of the disk mass is subjected to large uncertainties, that include systematic and method-of-computation uncertain-

ties. The leading trends in the data appears to be captured by the fitting formulae that include mass-ratio and reduced tidal deformability. This result is generally supported by the datasets separate statistical analysis (see Appendix B). As a simple polynomial in terms of mass ratio and the reduced tidal deformability shows similar or better residuals and χ_ν^2 , compared to other fitting formulae available in the literature and formulated in terms of other binary parameters, we conclude that the former two quantities describe the leading trends in data. The analysis of all datasets individually generally confirms this conclusion, further suggesting that both $P_2^2(q, \tilde{\Lambda})$ and Eq. (12) perform similarly well (see Appendix B).

V. DISCUSSION

In this paper we considered numerical relativity datasets available in the literature for the dynamical ejecta properties and the remnant disk mass from binary neutron star mergers. We performed a simple statistical analysis of the ejecta parameters that highlighted that the ejecta parameters are subjected to large systematic uncertainties, partially due to different treatment of neutrinos, in addition to the EOS formulations. We also compared different fitting formulae for the ejecta properties and disk mass and found that fitting formulae that include the reduced tidal parameter and mass ratio can relatively well reproduce the leading trends in certain datasets with more uniform physics input. In particular, low order polynomials in these quantities provide a simple description of the data available and also favorably compare to the other options in terms of sum of squared residuals when only models of `M0RefSet` are considered as well or models from all datasets. Large values of SSR and χ_ν^2 as well as wild oscillations of fitting coefficients for a given quantity between calibrations (see App. A) further indicate the limitations on the ability of the set of all simulations to preserve physical information. This calls for more detailed studies of error estimates in simulations containing the necessary physics. Additionally, a larger sample of simulations with parameters more uniformly distributed is required as the current set available in the literature is rather limited in terms of mass and mass-ratio, and mostly concentrated around binaries with fiducial $1.4M_\odot$ NS. Nonetheless, since these fitting formulas are widely used for multimessenger analyses, we propose the use of these polynomial models instead of other fitting formulae presented in the literature (and also considered in this work) because most of these formulae lead to ill-conditioned fits. Specifically, we recommend the Eq. (6) calibrated with datasets with the most advanced physics input, *i.e.*, `M0/M1Set` and `M0RefSet` (highlighted rows in Tab. IV and Tab. VI) We emphasize that the application of the fitting formulae, especially polynomials, should be limited to the parameter space where they have been calibrated. Additionally, while our analysis suggests that for

the currently available data, the second order polynomials in q and $\tilde{\Lambda}$ perform comparatively well, higher-order formulae might be necessary to capture the true physics of mergers. We leave their exploration to future works when more simulation data becomes available.

When all data from all available datasets are considered, the fitting formulae with the best statistical performance among those considered are able to reproduce the dynamical ejecta velocity typically to $\sim 50\%$, with the 68% significance range being $\Delta v_\infty/v_\infty \in (-0.4, 0.2)$. The electron fraction is reproduced with an accuracy of ~ 0.1 . The ejecta RMS half opening angle about the orbital plane is reproduced with an accuracy of ~ 10 deg. The ejecta and disk masses, however, are rather uncertain having $(-0.8, 0.2)$ and $(-0.4, 0.2)$ 68% significance ranges respectively. The smooth fitting formulae can reproduce these quantities to a factor of ~ 2 .

The main conclusion of this work is that the currently available data on the ejecta properties and disk masses from binary neutron star mergers contains large systematic uncertainties. Different treatments of EOS and neutrino transport, as well as different resolutions, and methods of calculation of ejecta and disk properties lead to large systematic differences between various datasets. As neutrino re-absorption is a crucial component for reliable estimates of the dynamical ejecta mass, *e.g.* [31, 41, 42, 82], it is of paramount importance to enlarge the `M0/M1Set` and refine the statistics of ejecta properties. Additionally, different methodologies used to extract and compute these quantities contribute to the uncertainties. Simulations of sequences of binaries at different chirp masses could also be useful to identify new trends in the data that cannot be currently explored. The statistical analysis that we have performed is further subjected to biases as the data in different datasets span different ranges in parameter space of the binary. Considerably larger sets of simulations that cover the parameter space more uniformly are needed to alleviate these biases.

Fitting formulae to the ejecta properties and disk mass are commonly used to study sources of the gravitational waves and electromagnetic counterparts. However, caution ought to be exercised when applying the fitting formulae presented here to infer the source parameters from observations.

As an example, we discuss the impact of using our recommended, $P_2^2(q, \tilde{\Lambda})$, fitting formula for the computation of synthetic kilonova light curves as opposed to the direct numerical relativity input⁵. We use the semi-analytic model of Ref. [31] with one or two kilonova components, *i.e.*, the dynamical ejecta and the disk wind. We consider a set of selected BNS models from the `M0RefSet` with 5 different EOS and several mass ratios between $q = 1.00$

⁵ The ejecta mass, velocity and electron fraction distributions are used to compute the light curve as in Ref. [75]

and $q = 1.82$. From the $P_2^2(q, \tilde{\Lambda})$ we estimate the dynamical ejecta mass and velocity and angle separating the low opacity polar part and high opacity part about the plane of the binary, using the θ_{RMS} as a separation angle. We invoke the ejecta mass-averaged RMS half opening angle to separate the low-altitude high opacity part and the low-opacity polar part. This allows us to include the change in ejecta geometry with binary parameters. For the secular ejecta mass we assume it to be 40% of the disk mass, evaluated from the best fitting formula. The opacities, heating rates and extrinsic parameters are kept fixed in the comparison.

The results are collected in Fig. 10, where we show peak times and peak magnitudes for the g , z , and K_s filters. In the one component case (left panels), we find that the peak times are reproduced on average within ~ 0.2 days in the g and z bands, and within ~ 0.5 days in K_s band. The latter is systematically underestimated. The highly asymmetric binary $q = 1.8$ and BLh EOS shows overall the largest deviations. Peak magnitudes in the three bands computed with the fitting formulae differ by ~ 0.5 mag from the NR informed ones, reaching ~ 1 mag in the g band. In the two component case (right panels) the peak times in the K_s band based on the best fitting formulae are more uncertain and amount to ~ 2 days. The peak magnitude show deviations of $\sim \pm 0.5$ mag in z and K_s bands. The reason why the peak magnitudes are more uncertain in the one component case lies in the complex geometry that are inherited in kilonova models from the numerical relativity data, but is not sufficiently well captured by the single parameter, mass-averaged RMS half opening angle, considered here. While the precise details and origin of these differences can be related to the specific light curve model employed here, this example indicates the minimum systematic variation is to be expected in the light curve predictions when using our recommended fitting formula.

ACKNOWLEDGMENTS

We thank the anonymous referees for their comments that helped us improve the manuscript. We thank Erika Holmbeck for useful discussions. S.B., B.D. and F.Z. acknowledge support by the EU H2020 under ERC Starting Grant, no. BinGraSp-714626. D.R. acknowledges support from the U.S. Department of Energy, Office of Science, Division of Nuclear Physics under Award Number(s) DE-SC0021177 and from the National Science Foundation under Grant No. PHY-2011725. Data post-processing was performed on the Virgo ‘‘Tullio’’ server at Torino supported by INFN.

Appendix A: Tables with fitting coefficients

This appendix summarizes all fit coefficients. Dynamical ejecta coefficients can be found in Tab. IV and

Tab. V for the polynomials and fitting formulae respectively. Disk coefficients can be found in Tab VI and Tab. VII for the polynomials and fitting formulae respectively. The coefficients of the recommended fitting formulae, as discussed in the conclusion, are highlighted in the tables. Importantly, the range of the binary parameters of the datasets used for calibration ought to be taken into account when the fitting formulae are used. The corresponding ranges are discussed in Sec.II.

Appendix B: Statistics for individual datasets

In this appendix we discuss the SSR and χ_ν^2 statistics of all fitting formulae dataset-wise instead of adding them up, as was done in the main text. In Tab. VIII we compare the different fits for the dynamical ejecta properties and disk mass in terms of the SSR, and in the Fig. 11 we show the residuals of the $P_2^2(q, \tilde{\Lambda})$, with different calibrations for ejecta mass and disk mass.

Regarding the ejecta mass we find that $P_2^2(q, \tilde{\Lambda})$ and Eq. (8) display the lowest SSR. While for **M0RefSet** and **NoNusSet** the $P_2^2(q, \tilde{\Lambda})$ is preferred, for the other two datasets, the Eq. (8) gives slightly lower SSR. Additionally we note that the datasets that are more uniform in their physics and method, *e.g.*, **M0RefSet** and **LeakSet** display the lowest χ_ν^2 . The largest χ_ν^2 is found for the **M0/M1Set**, that incorporates both, models with M1 and leakage+M0 neutrino schemes. Notably, (7) shows similar values of χ_ν^2 for **M0/M1Set**, **M0RefSet** and **LeakSet**. Fig. 11 also shows that the $P_2^2(q, \tilde{\Lambda})$ reproduces the models of **M0/M1Set**, **LeakSet** and **NoNusSet** less robustly than those of **M0RefSet**. In part this is due to the limited $\tilde{\Lambda}$ range of models of **M0RefSet** and fixed chirp mass, and in part it hints at the systematic uncertainties due to different physics setup of simulations.

For the ejecta velocity, the $P_2^2(q, \tilde{\Lambda})$ gives the lowest SSR for all datasets. Meanwhile, the largest χ_ν^2 is found for the **LeakSet** across all fitting formulae. This might be attributed to the systematic uncertainties that pure leakage neutrino scheme introduces for models with different outcomes, *e.g.*, prompt collapse and stable remnants.

With respect to ejecta electron fraction and RMS half opening angle, $P_2^2(q, \tilde{\Lambda})$ gives significantly lower SSR than $P_2^1(\tilde{\Lambda})$ and the difference in χ_ν^2 are small. Notably, for the $\langle Y_e \rangle$, the χ_ν^2 is similar between the **M0RefSet** and **M0/M1Set**. This indicates the consistency in neutrino reabsorption effects on the ejecta composition in these datasets.

For the disk mass we find that the lowest SSR is given $P_2^2(q, \tilde{\Lambda})$ for all datasets. The largest χ_ν^2 is found for **M0RefSet** and the smallest for **M0/M1Set**. The reason for that is largely due to the error measure that we use to compute the χ_ν^2 . For instance, if we employ the error bars for the **M0RefSet** individually for each model (See Tab. 1 in [34]), we obtain $\chi_\nu^2 \sim 1$. However, this information is not available for other datasets and the uniform error measure, Eq. (3) was chosen for consistency. The Fig. 11

TABLE IV. Dynamical ejecta properties: coefficients for polynomial regression of various quantities. Results for both first order and second order polynomials are reported $P_1^2(\tilde{\Lambda})$ and $P_2^2(q, \tilde{\Lambda})$. The recommended calibration for $P_2^2(q, \Lambda)$ is highlighted.

Quantity	Datasets	b_0	b_1	b_2	b_3	b_4	b_5	χ_ν^2
$\log_{10}(M_{\text{ej}})$	MORefSet	-3.49	3.51×10^{-3}	-3.01×10^{-6}				1.9
	& MO/M1Set	-2.40	-7.11×10^{-5}	-1.60×10^{-7}				18.8
	& LeakSet	-3.37	1.85×10^{-3}	-1.21×10^{-6}				14.3
	& NoNusSet	-2.53	-2.03×10^{-5}	-6.74×10^{-9}				46.0
v_∞ [c]	MORefSet	4.28×10^{-1}	-8.46×10^{-4}	6.42×10^{-7}				2.9
	& MO/M1Set	3.37×10^{-1}	-4.70×10^{-4}	3.16×10^{-7}				3.2
	& LeakSet	2.75×10^{-1}	-2.36×10^{-4}	1.39×10^{-7}				6.2
	& NoNusSet	2.50×10^{-1}	-6.66×10^{-5}	2.15×10^{-8}				7.6
Y_e	MORefSet	3.26×10^{-1}	-6.16×10^{-4}	5.70×10^{-7}				42.7
	& MO/M1Set	1.98×10^{-1}	-3.05×10^{-5}	4.64×10^{-8}				38.3
	& LeakSet	1.45×10^{-1}	1.09×10^{-4}	-6.89×10^{-8}				36.0
$\langle \theta_{\text{RMS}} \rangle$ [deg]	MORefSet	$3.95 \times 10^{+1}$	-4.96×10^{-2}	5.00×10^{-5}				21.2
	& MO/M1Set	2.41×10^1	7.21×10^{-3}	2.28×10^{-6}				18.3
	& LeakSet	1.44×10^1	3.42×10^{-2}	-1.81×10^{-5}				14.1
$\log_{10}(M_{\text{ej}})$	MORefSet	0.436	-2.75	-6.18×10^{-3}	2.75×10^{-1}	4.78×10^{-3}	3.96×10^{-7}	1.2
	& MO/M1Set	-1.32	-3.82×10^{-1}	-4.47×10^{-3}	-3.39×10^{-1}	3.21×10^{-3}	4.31×10^{-7}	20.8
	& LeakSet	-6.96	5.26	7.84×10^{-4}	-1.71	5.69×10^{-4}	-9.09×10^{-7}	7.9
	& NoNusSet	-6.01	4.91	-1.24×10^{-3}	-1.57	1.00×10^{-3}	2.77×10^{-8}	17.9
v_∞ [c]	MORefSet	6.10×10^{-1}	-1.12×10^{-1}	-1.04×10^{-3}	-6.56×10^{-2}	3.56×10^{-4}	4.25×10^{-7}	0.9
	& MO/M1Set	5.94×10^{-1}	-1.48×10^{-1}	-8.62×10^{-4}	-5.02×10^{-2}	3.25×10^{-4}	3.16×10^{-7}	1.6
	& LeakSet	2.55×10^{-1}	1.88×10^{-1}	-4.44×10^{-4}	-1.46×10^{-1}	1.87×10^{-4}	1.38×10^{-7}	5.3
	& NoNusSet	3.46×10^{-1}	-8.11×10^{-2}	-8.11×10^{-5}	-3.67×10^{-3}	8.89×10^{-6}	1.99×10^{-8}	7.0
Y_e	MORefSet	-3.49×10^{-2}	3.01×10^{-1}	5.55×10^{-4}	-1.52×10^{-1}	-2.06×10^{-4}	-2.44×10^{-7}	8.7
	& MO/M1Set	2.55×10^{-1}	3.83×10^{-2}	2.36×10^{-4}	-6.66×10^{-2}	-1.92×10^{-4}	-1.86×10^{-8}	9.6
	& LeakSet	-2.58×10^{-1}	6.33×10^{-1}	5.02×10^{-4}	-2.41×10^{-1}	-3.04×10^{-4}	-1.25×10^{-7}	24.8
$\langle \theta_{\text{RMS}} \rangle$ [deg]	MORefSet	-7.79×10^1	1.38×10^2	1.30×10^{-1}	-5.50×10^1	-3.33×10^{-2}	-7.25×10^{-5}	4.4
	& MO/M1Set	-5.61×10^1	1.29×10^2	6.88×10^{-2}	-5.27×10^1	-2.72×10^{-2}	-2.78×10^{-5}	4.1
	& LeakSet	-1.06×10^2	1.79×10^2	1.11×10^{-1}	$-6.10 \times 10^{+1}$	-6.59×10^{-2}	-2.48×10^{-5}	8.5

TABLE V. Dynamical ejecta properties: coefficients for the fitting formulae discussed in the text for various datasets.

Quantity	Fit	Datasets	α	β	γ	δ	n	χ_ν^2
$\log_{10}(M_{\text{ej}})$	Eq. (7)	MORefSet	9.662×10^{-2}	1.037	5.034	-8.316	2.432×10^{-1}	1.6
		& MO/M1Set	-1.004×10^{-1}	-4.403×10^{-1}	-6.452×10^{-1}	2.696×10^{-1}	3.222×10^{-1}	6.0
		& LeakSet	-1.067×10^{-1}	-1.651	2.806	2.784	3.013×10^{-1}	13.6
		& NoNusSet	9.429×10^{-2}	-7.036×10^{-1}	2.121	-1.026	5.328×10^{-1}	29.9
$\log_{10}(M_{\text{ej}})$	Eq. (8)	MORefSet	-2.361×10^{-3}	2.750×10^{-2}	-8.573×10^{-2}		1.279	1.4
		& MO/M1Set	-1.261×10^{-3}	1.449×10^{-2}	-4.715×10^{-2}		1.306	5.1
		& LeakSet	-1.153×10^{-3}	1.285×10^{-2}	-4.164×10^{-2}		1.339	6.1
		& NoNusSet	-3.351×10^{-4}	2.697×10^{-3}	-9.738×10^{-3}		1.729	20.0
v_∞ [c]	Eq. (9)	MORefSet	-7.242×10^{-1}	1.279	-1.537			1.2
		& MO/M1Set	-5.631×10^{-01}	1.109	-1.186			2.3
		& LeakSet	-4.007×10^{-1}	9.164×10^{-1}	-6.881×10^{-1}			6.0
		& NoNusSet	-3.627×10^{-1}	8.191×10^{-1}	-1.128			6.8

shows that indeed, the $P_2^2(q, \tilde{\Lambda})$ reproduces the data of MO/M1Set much better than of any other dataset, with lower residuals. This can be attributed to the fact that models of MO/M1Set span a more narrow range in mass ratios and does not include prompt collapse models that can lead to either massive disks in very asymmetric binaries [68] or a negligible disks in equal mass but massive ones [64].

Overall, the datasets-wise statistical analysis of ejecta properties and disk mass shows the same qualitative pic-

ture reported in the main text.

Appendix C: Effect of the error measure on the fitting procedure results

In the main text, the comparison between different fitting formulae and their respective calibration is performed using residuals (SSR). Additionally we discuss the χ_ν^2 using the error measures found in the literature.

TABLE VI. Disk mass: coefficients for polynomial regression of various quantities. Results for both first order and second order polynomials are reported $P_2^1(\tilde{\Lambda})$ and $P_2^2(q, \tilde{\Lambda})$. The recommended calibration for $P_2^2(q, \tilde{\Lambda})$ is highlighted. Note, that here the \log_{10} of the RHS of respective polynomials is considered.

Datasets	b_0	b_1	b_2	b_3	b_4	b_5	χ_ν^2
MORefSet	-3.62×10^{-1}	1.42×10^{-3}	-9.60×10^{-7}				477.8
& MO/M1Set	-1.76×10^{-1}	7.50×10^{-4}	-4.01×10^{-7}				323.6
& LeakSet	3.53×10^{-2}	-3.12×10^{-4}	6.88×10^{-7}				37.3
& NoNusSet	1.05×10^{-2}	-1.44×10^{-4}	4.99×10^{-7}				61.0
MORefSet	-1.80	2.44	7.87×10^{-4}	-6.78×10^{-1}	-8.08×10^{-4}	2.80×10^{-7}	8.8
& MO/M1Set	-1.85	2.59	7.07×10^{-4}	-7.33×10^{-1}	-8.08×10^{-4}	2.75×10^{-7}	26.6
& LeakSet	-1.26	1.76	3.51×10^{-4}	-4.82×10^{-1}	-5.20×10^{-4}	3.68×10^{-7}	18.9
& NoNusSet	-5.10×10^{-1}	7.78×10^{-1}	-3.29×10^{-4}	-2.60×10^{-1}	2.33×10^{-4}	2.92×10^{-7}	18.1

TABLE VII. Disk mass: coefficients for the fitting formulae discussed in the text for various datasets.

Fit	Datasets	α	β	γ	δ	χ_ν^2
Eq. (11)	MORefSet	9.958×10^{-2}	5.346×10^{-2}	4.793×10^2	6.106	298.4
	& MO/M1Set	1.026×10^{-1}	5.095×10^{-2}	4.710×10^2	5.351×10^{-1}	203.0
	& LeakSet	7.677×10^{-2}	8.752×10^{-2}	5.835×10^2	3.429×10^2	105.1
	& NoNusSet	7.656×10^{-2}	8.765×10^{-2}	5.840×10^2	3.474×10^2	75.0
Eq. (12)	MORefSet	-6.852	1.191	1.346		25.5
	& MO/M1Set	-7.184	1.303	1.613		55.4
	& LeakSet	-5.217	0.902	1.090		18.8
	& NoNusSet	-8.963	1.769	2.841		39.3

TABLE VIII. Sum of squared residuals, SSR, for different fitting models for the dynamical ejecta properties and disk mass (see descriptions of the Tab. II and Tab. III). Here datasets are not added, but considered individually.

$\log_{10}(M_{\text{ej}})$	Datasets	N	Mean	Eq. (7)	Eq. (8)	$P_2^1(\tilde{\Lambda})$	$P_2^2(q, \tilde{\Lambda})$
	MORefSet	34	2.57	1.65	1.40	2.43	0.97
	MO/M1Set	30	5.56	3.32	4.35	5.04	4.49
	LeakSet	42	12.70	10.24	9.73	11.36	10.64
	NoNusSet	165	43.74	25.78	25.57	43.35	20.40
$\langle v_{\text{ej}} \rangle$	Datasets	N	Mean	Eq. (9)		$P_2^1(\tilde{\Lambda})$	$P_2^2(q, \tilde{\Lambda})$
	MORefSet	34	0.04	0.02		0.04	0.01
	MO/M1Set	27	0.04	0.03		0.03	0.02
	LeakSet	42	0.17	0.17		0.16	0.14
	NoNusSet	143	0.40	0.30		0.33	0.29
$\langle Y_e \rangle$	Datasets	N	Mean			$P_2^1(\tilde{\Lambda})$	$P_2^2(q, \tilde{\Lambda})$
	MORefSet	34	0.14			0.13	0.02
	MO/M1Set	30	0.05			0.05	0.02
	LeakSet	35	0.04			0.04	0.04
$\langle \theta_{\text{RMS}} \rangle$	Datasets	N	Mean			$P_2^1(\tilde{\Lambda})$	$P_2^2(q, \tilde{\Lambda})$
	MORefSet	34	2775			2631	498
	MO/M1Set	7	54			49	30
	LeakSet	35	1355			1048	843
M_{disk}	Dataset	N	Mean	Eq. (11)	Eq. (12)	$P_2^1(\tilde{\Lambda})$	$P_2^2(q, \tilde{\Lambda})$
	MORefSet	31	15.11	13.28	9.96	13.95	8.81
	MO/M1Set	23	1.88	0.93	0.59	1.18	0.44
	LeakSet	26	28.33	14.42	6.85	6.73	6.36
	NoNusSet	39	25.66	12.08	4.24	10.37	5.14

In this appendix we investigate how different error measures and different criteria for fitting procedure affect the result. We focus on the models of MORefSet only, for which we have errors estimated directly from the numerical relativity (NR) simulations performed at

different resolutions (See Table 1 in [34]). We also limit the analysis to the $P_2^2(q, \tilde{\Lambda})$ fitting formula. We consider three approaches: (i) minimizing the residuals, (ii) minimizing the χ_ν^2 with the default errors, discussed in the main text and (iii) minimizing χ_ν^2 with the NR-informed errors. For the (i) we compute two χ_ν^2 , computed for both error measures.

For the M_{ej} we observe that for (i) the χ_ν^2 increases by almost 3 orders of magnitude when employing the NR-informed errors from 1.17 to 563.92. Meanwhile, the difference in the quality of the fit computed with minimization of χ_ν^2 using these two error measures, *i.e.*, (ii) and (iii), changes only slightly, as Fig. 12 shows. As expected, the extrema of $\Delta M_{\text{ej}}/M_{\text{ej}}$ are the lowest, $(-2.34, 0.54)$ when the residuals are minimize. However, even when χ_ν^2 is minimized, the increase in extrema is not significant (with respect to the overall fit performance): $(-2.73, 0.50)$ for default error measure and $(-2.60, 0.51)$ for NR-informed errors.

For the $\langle v_\infty \rangle$, we observe no difference between the fit calibrated minimizing residuals (i) or minimizing χ_ν^2 with default error (ii), as the error measure is a constant value. However, the increase in χ_ν^2 amounts to an order of a magnitude from 0.9 to 9.3. When the NR-informed error is used the fit changes slightly at the lower tail of the velocity with the decrease in χ_ν^2 to 3.3.

Similar behaviour is observed for the $\langle Y_e \rangle$ and $\langle \theta_{\text{RMS}} \rangle$ as the error measure for these quantities are also constants.

For the M_{disk} we observe the similar picture as for the M_{ej} . For (i) the χ_ν^2 increases by $\gtrsim 3$ orders of magni-

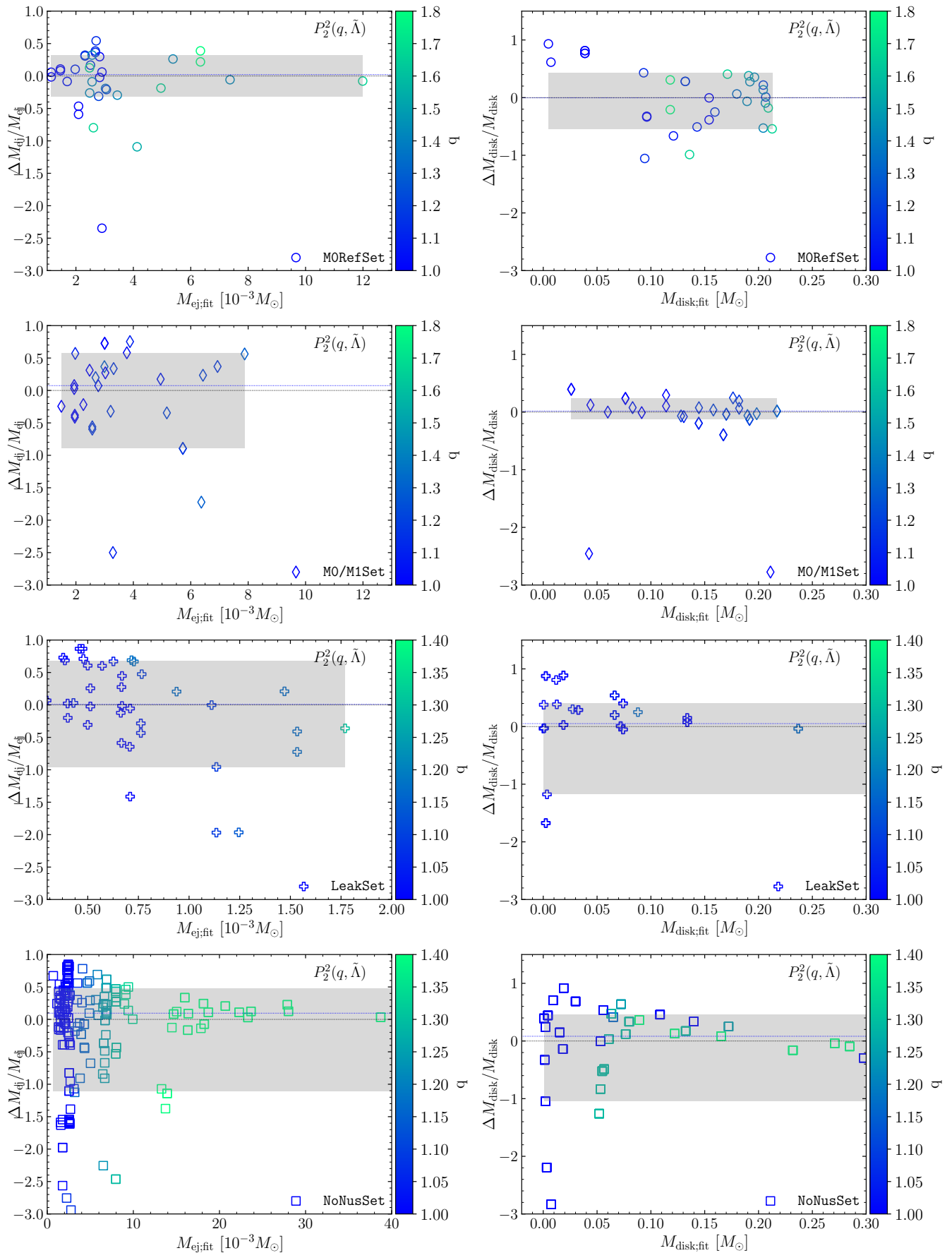


FIG. 11. Comparison between the data and values obtained from the fitting formula $P_2^2(q, \tilde{\Lambda})$ for the ejecta mass (*left column of plots*) and disk mass (*right column of plots*). The plot is similar to the 2 and 8, but instead of showing the result for the combined dataset with all models, in each panel only one dataset is used to calibrate the $P_2^2(q, \tilde{\Lambda})$ fitting formula.

tude from 1.5 to 192. However, the difference in the fit quantitative performance with minimization of χ_ν^2 using the two error measures, *i.e.*, (ii) and (iii), remains within data points' error bars (see Fig. 12, left panel).

For a fixed $q = 1$ the performance of the $P_2^2(q, \tilde{\Lambda})$ is shown in Fig. 13. We observe that the largest difference in both cases amounts to 0.25 in \log_{10} of the respective quantity. The fit computed minimizing the χ_ν^2 gives higher values across the considered range of $\tilde{\Lambda}$.

The qualitative behavior of the fits remain, however, unchanged.

That the outcome of the fit calibration depends on the choice of the error measure only when this measure is biased. Otherwise, it is equivalent to minimizing residuals,

as is the case for all quantities considered except masses. Regarding the latter, while the qualitative behavior of the fit appears to be independent of the minimization technique, the quantitative difference is present. The error measures considered in the main text are motivated by the finite-resolution errors found in numerical simulations [64]. However, their use for the statistical analysis of different datasets performed with different physics and numerical setups might not be optimal. This was our motivation to minimize residuals in the fitting formulae analysis in the main text. Employing a more physically and statistically motivated error measure in future analysis, when larger sample of data is available, would lead to better constrained fits.

-
- [1] I. Arcavi *et al.*, *Nature* **551**, 64 (2017), arXiv:1710.05843 [astro-ph.HE].
- [2] D. A. Coulter *et al.*, *Science* (2017), 10.1126/science.aap9811, [Science358,1556(2017)], arXiv:1710.05452 [astro-ph.HE].
- [3] M. R. Drout *et al.*, (2017), 10.1126/science.aaq0049, arXiv:1710.05443 [astro-ph.HE].
- [4] P. A. Evans *et al.*, (2017), 10.1126/science.aap9580, arXiv:1710.05437 [astro-ph.HE].
- [5] G. Hallinan *et al.*, (2017), 10.1126/science.aap9855, arXiv:1710.05435 [astro-ph.HE].
- [6] M. M. Kasliwal *et al.*, (2017), 10.1126/science.aap9455, arXiv:1710.05436 [astro-ph.HE].
- [7] M. Nicholl *et al.*, *Astrophys. J.* **848**, L18 (2017), arXiv:1710.05456 [astro-ph.HE].
- [8] S. J. Smartt *et al.*, *Nature* (2017), 10.1038/nature24303, arXiv:1710.05841 [astro-ph.HE].
- [9] M. Soares-Santos *et al.* (DES), *Astrophys. J.* **848**, L16 (2017), arXiv:1710.05459 [astro-ph.HE].
- [10] N. R. Tanvir *et al.*, *Astrophys. J.* **848**, L27 (2017), arXiv:1710.05455 [astro-ph.HE].
- [11] E. Troja *et al.*, *Nature* (2017), 10.1038/nature24290, arXiv:1710.05433 [astro-ph.HE].
- [12] K. P. Mooley, A. T. Deller, O. Gottlieb, E. Nakar, G. Hallinan, S. Bourke, D. A. Frail, A. Horesh, A. Corsi, and K. Hotokezaka, *Nature* **561**, 355 (2018), arXiv:1806.09693 [astro-ph.HE].
- [13] J. J. Ruan, M. Nynka, D. Haggard, V. Kalogera, and P. Evans, *Astrophys. J.* **853**, L4 (2018), arXiv:1712.02809 [astro-ph.HE].
- [14] J. D. Lyman *et al.*, *Nat. Astron.* **2**, 751 (2018), arXiv:1801.02669 [astro-ph.HE].
- [15] B. P. Abbott *et al.* (Virgo, LIGO Scientific), *Astrophys. J.* **850**, L39 (2017), arXiv:1710.05836 [astro-ph.HE].
- [16] B. P. Abbott *et al.* (Virgo, LIGO Scientific), *Phys. Rev. Lett.* **119**, 141101 (2017), arXiv:1709.09660 [gr-qc].
- [17] B. P. Abbott *et al.* (LIGO Scientific, Virgo), *Phys. Rev.* **X9**, 011001 (2019), arXiv:1805.11579 [gr-qc].
- [18] B. P. Abbott *et al.* (LIGO Scientific, Virgo), (2018), 10.3847/1538-4357/ab0f3d, arXiv:1810.02581 [gr-qc].
- [19] J. M. Lattimer and D. N. Schramm, *Astrophys. J. Letters* **192**, L145 (1974).
- [20] E. Symbalisty and D. N. Schramm, *Astrophys. J. Letters* **22**, 143 (1982).
- [21] L.-X. Li and B. Paczynski, *Astrophys. J.* **507**, L59 (1998), arXiv:astro-ph/9807272 [astro-ph].
- [22] S. R. Kulkarni, (2005), arXiv:astro-ph/0510256 [astro-ph].
- [23] S. Rosswog, M. Liebendoerfer, F. Thielemann, M. Davies, W. Benz, *et al.*, *Astron. Astrophys.* **341**, 499 (1999), arXiv:astro-ph/9811367 [astro-ph].
- [24] S. Rosswog, *Astrophys. J.* **634**, 1202 (2005), arXiv:astro-ph/0508138 [astro-ph].
- [25] B. Metzger, G. Martinez-Pinedo, S. Darbha, E. Quataert, A. Arcones, *et al.*, *Mon. Not. Roy. Astron. Soc.* **406**, 2650 (2010), arXiv:1001.5029 [astro-ph.HE].
- [26] L. F. Roberts, D. Kasen, W. H. Lee, and E. Ramirez-Ruiz, *Astrophys. J.* **736**, L21 (2011), arXiv:1104.5504 [astro-ph.HE].
- [27] D. Kasen, N. R. Badnell, and J. Barnes, *Astrophys. J.* **774**, 25 (2013), arXiv:1303.5788 [astro-ph.HE].
- [28] P. S. Cowperthwaite *et al.*, *Astrophys. J.* **848**, L17 (2017), arXiv:1710.05840 [astro-ph.HE].
- [29] V. A. Villar *et al.*, *Astrophys. J.* **851**, L21 (2017), arXiv:1710.11576 [astro-ph.HE].
- [30] M. Tanaka *et al.*, *Publ. Astron. Soc. Jap.* (2017), 10.1093/pasj/psx121, arXiv:1710.05850 [astro-ph.HE].
- [31] A. Perego, D. Radice, and S. Bernuzzi, *Astrophys. J.* **850**, L37 (2017), arXiv:1711.03982 [astro-ph.HE].
- [32] K. Kawaguchi, M. Shibata, and M. Tanaka, *Astrophys. J.* **865**, L21 (2018), arXiv:1806.04088 [astro-ph.HE].
- [33] S. Fahlman and R. Fernández, *Astrophys. J.* **869**, L3 (2018), arXiv:1811.08906 [astro-ph.HE].
- [34] V. Nedora, S. Bernuzzi, D. Radice, B. Daszuta, A. Endrizzi, A. Perego, A. Prakash, M. Safarzadeh, F. Sichi-anchi, and D. Logoteta, *Astrophys. J.* **906**, 98 (2021), arXiv:2008.04333 [astro-ph.HE].
- [35] B. D. Metzger, *Living Rev. Rel.* **23**, 1 (2020), arXiv:1910.01617 [astro-ph.HE].
- [36] M. Shibata and K. Hotokezaka, *Ann. Rev. Nucl. Part. Sci.* **69**, 41 (2019), arXiv:1908.02350 [astro-ph.HE].
- [37] D. Radice, S. Bernuzzi, and A. Perego, *Ann. Rev. Nucl. Part. Sci.* **70** (2020), 10.1146/annurev-nucl-013120-114541, arXiv:2002.03863 [astro-ph.HE].
- [38] S. Bernuzzi, *Gen. Rel. Grav.* **52**, 108 (2020), arXiv:2004.06419 [astro-ph.HE].
- [39] K. Hotokezaka, K. Kiuchi, K. Kyutoku, T. Muranushi, Y.-i. Sekiguchi, *et al.*, *Phys. Rev.* **D88**, 044026 (2013),

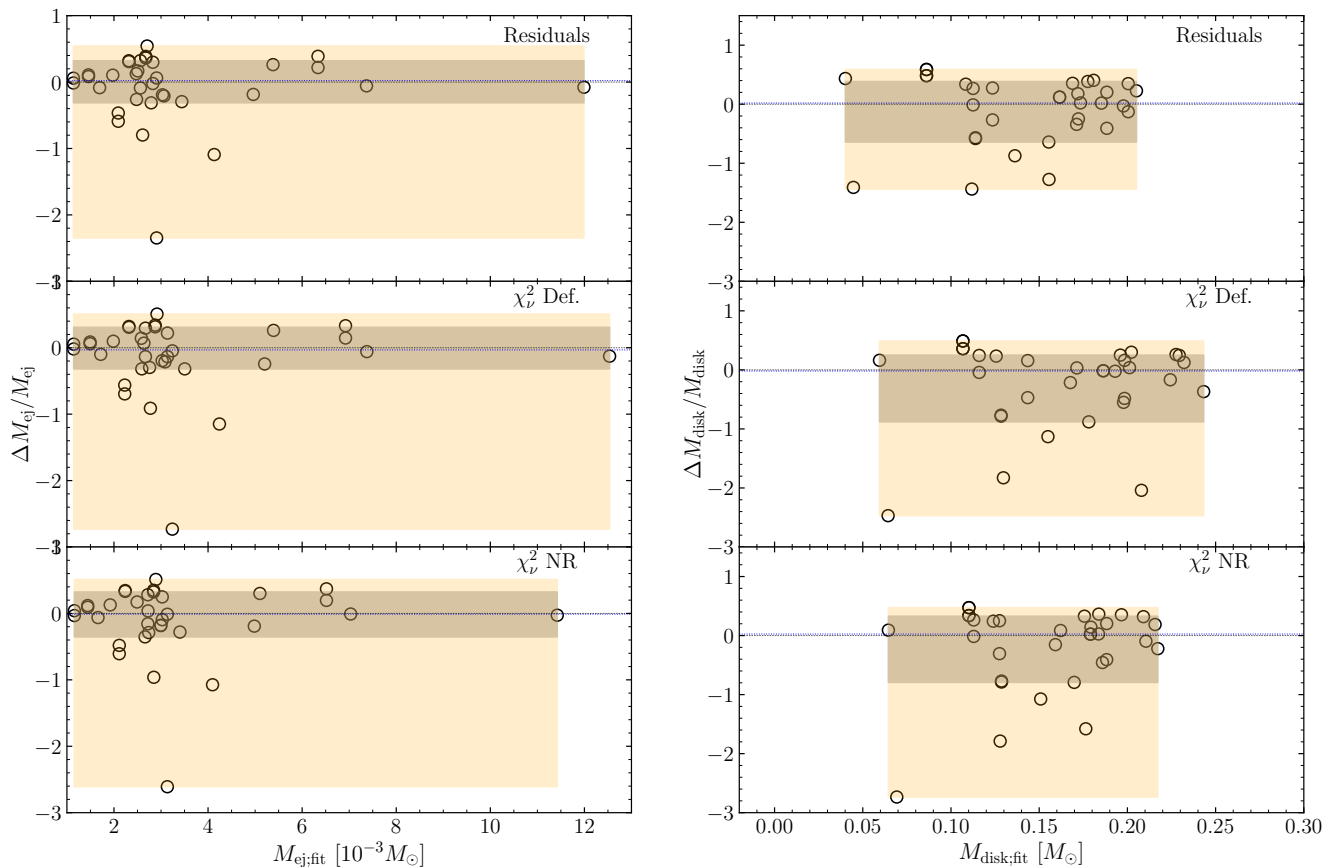


FIG. 12. Effects of different calibration methods for $P_2^2(q, \bar{\Lambda})$ fit for models of **M0RefSet** for the ejecta mass (*left panel*) and disk mass (*right panel*). We consider the minimization of residuals, χ_ν^2 with default error measures (Eqs. (2),(3)), and the errors estimated from multi-resolution analysis in [34]. Gray / pastel shaded regions mark the 1σ (68%) / 2σ (95.4%) confidence intervals.

- arXiv:1307.5888 [astro-ph.HE].
- [40] A. Bauswein, S. Goriely, and H.-T. Janka, *Astrophys.J.* **773**, 78 (2013), arXiv:1302.6530 [astro-ph.SR].
- [41] S. Wanajo, Y. Sekiguchi, N. Nishimura, K. Kiuchi, K. Kyutoku, and M. Shibata, *Astrophys. J.* **789**, L39 (2014), arXiv:1402.7317 [astro-ph.SR].
- [42] Y. Sekiguchi, K. Kiuchi, K. Kyutoku, and M. Shibata, *Phys.Rev.* **D91**, 064059 (2015), arXiv:1502.06660 [astro-ph.HE].
- [43] D. Radice, F. Galeazzi, J. Lippuner, L. F. Roberts, C. D. Ott, and L. Rezzolla, *Mon. Not. Roy. Astron. Soc.* **460**, 3255 (2016), arXiv:1601.02426 [astro-ph.HE].
- [44] Y. Sekiguchi, K. Kiuchi, K. Kyutoku, M. Shibata, and K. Taniguchi, *Phys. Rev.* **D93**, 124046 (2016), arXiv:1603.01918 [astro-ph.HE].
- [45] T. Vincent, F. Foucart, M. D. Duez, R. Haas, L. E. Kidder, H. P. Pfeiffer, and M. A. Scheel, *Phys. Rev.* **D101**, 044053 (2020), arXiv:1908.00655 [gr-qc].
- [46] L. Dessart, C. Ott, A. Burrows, S. Rosswog, and E. Livne, *Astrophys.J.* **690**, 1681 (2009), arXiv:0806.4380 [astro-ph].
- [47] R. Fernández, E. Quataert, J. Schwab, D. Kasen, and S. Rosswog, *Mon. Not. Roy. Astron. Soc.* **449**, 390 (2015), arXiv:1412.5588 [astro-ph.HE].
- [48] A. Perego, S. Rosswog, R. Cabezon, O. Korobkin, R. Kaeppeli, *et al.*, *Mon.Not.Roy.Astron.Soc.* **443**, 3134 (2014), arXiv:1405.6730 [astro-ph.HE].
- [49] O. Just, A. Bauswein, R. A. Pulpillo, S. Goriely, and H. T. Janka, *Mon. Not. Roy. Astron. Soc.* **448**, 541 (2015), arXiv:1406.2687 [astro-ph.SR].
- [50] D. Kasen, R. Fernández, and B. Metzger, *Mon. Not. Roy. Astron. Soc.* **450**, 1777 (2015), arXiv:1411.3726 [astro-ph.HE].
- [51] B. D. Metzger and R. Fernández, *Mon.Not.Roy.Astron.Soc.* **441**, 3444 (2014), arXiv:1402.4803 [astro-ph.HE].
- [52] D. Martin, A. Perego, A. Arcones, F.-K. Thielemann, O. Korobkin, and S. Rosswog, *Astrophys. J.* **813**, 2 (2015), arXiv:1506.05048 [astro-ph.SR].
- [53] M.-R. Wu, R. Fernández, G. Martínez-Pinedo, and B. D. Metzger, *Mon. Not. Roy. Astron. Soc.* **463**, 2323 (2016), arXiv:1607.05290 [astro-ph.HE].
- [54] D. M. Siegel and B. D. Metzger, *Phys. Rev. Lett.* **119**, 231102 (2017), arXiv:1705.05473 [astro-ph.HE].
- [55] S. Fujibayashi, K. Kiuchi, N. Nishimura, Y. Sekiguchi, and M. Shibata, *Astrophys. J.* **860**, 64 (2018), arXiv:1711.02093 [astro-ph.HE].
- [56] B. D. Metzger, T. A. Thompson, and E. Quataert, *Astrophys. J.* **856**, 101 (2018), arXiv:1801.04286 [astro-ph.HE].

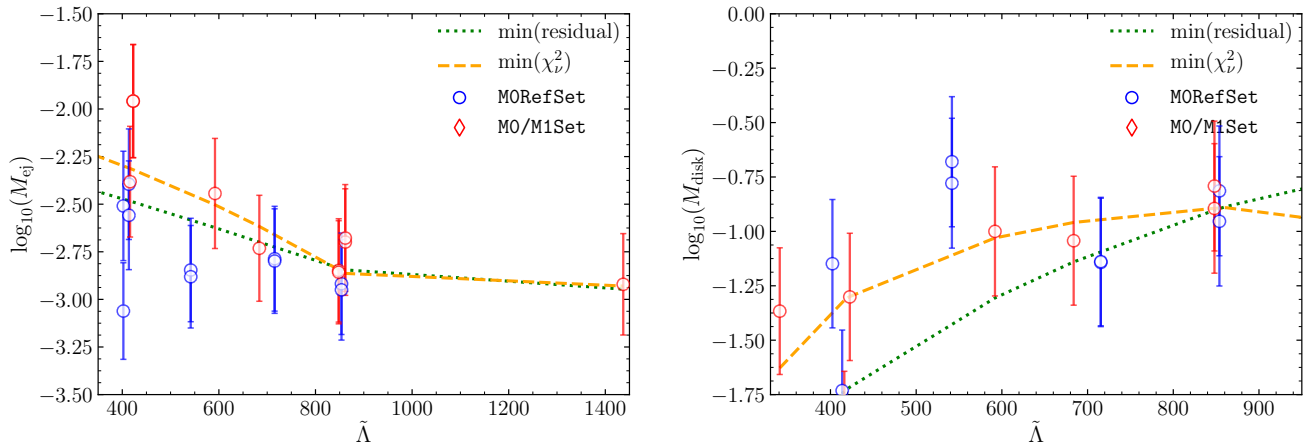


FIG. 13. Visual representation of the $P_2^2(q, \tilde{\Lambda})$ fit for ejecta mass (*left panel*) and disk mass (*right panel*). The fits are calibrated with M0/M1Set and M0RefSet, however, only models with $q = 1$ are plotted. The fit calibration is done either minimizing residuals or χ^2_ν . In the latter case, the default errors are used (and also plotted) namely, Eq. (2) and Eq. (3)

- [57] R. Fernández, A. Tchekhovskoy, E. Quataert, F. Foucart, and D. Kasen, *Mon. Not. Roy. Astron. Soc.* **482**, 3373 (2019), arXiv:1808.00461 [astro-ph.HE].
- [58] J. M. Miller, B. R. Ryan, J. C. Dolence, A. Burrows, C. J. Fontes, C. L. Fryer, O. Korobkin, J. Lippuner, M. R. Mumpower, and R. T. Wollaeger, *Phys. Rev.* **D100**, 023008 (2019), arXiv:1905.07477 [astro-ph.HE].
- [59] K. Hotokezaka, K. Kiuchi, K. Kyutoku, H. Okawa, Y.-i. Sekiguchi, *et al.*, *Phys. Rev.* **D87**, 024001 (2013), arXiv:1212.0905 [astro-ph.HE].
- [60] T. Dietrich, S. Bernuzzi, M. Ujevic, and B. Brügmann, *Phys. Rev.* **D91**, 124041 (2015), arXiv:1504.01266 [gr-qc].
- [61] C. Palenzuela, S. L. Liebling, D. Neilsen, L. Lehner, O. L. Caballero, E. O’Connor, and M. Anderson, *Phys. Rev.* **D92**, 044045 (2015), arXiv:1505.01607 [gr-qc].
- [62] S. Bernuzzi, D. Radice, C. D. Ott, L. F. Roberts, P. Moesta, and F. Galeazzi, *Phys. Rev.* **D94**, 024023 (2016), arXiv:1512.06397 [gr-qc].
- [63] L. Lehner, S. L. Liebling, C. Palenzuela, O. L. Caballero, E. O’Connor, M. Anderson, and D. Neilsen, *Class. Quant. Grav.* **33**, 184002 (2016), arXiv:1603.00501 [gr-qc].
- [64] D. Radice, A. Perego, K. Hotokezaka, S. A. Fromm, S. Bernuzzi, and L. F. Roberts, *Astrophys. J.* **869**, 130 (2018), arXiv:1809.11161 [astro-ph.HE].
- [65] A. Perego, S. Bernuzzi, and D. Radice, *Eur. Phys. J.* **A55**, 124 (2019), arXiv:1903.07898 [gr-qc].
- [66] K. Kiuchi, K. Kyutoku, M. Shibata, and K. Taniguchi, *Astrophys. J.* **876**, L31 (2019), arXiv:1903.01466 [astro-ph.HE].
- [67] A. Endrizzi, A. Perego, F. M. Fabbri, L. Branca, D. Radice, S. Bernuzzi, B. Giacomazzo, F. Pedriva, and A. Lovato, *Eur. Phys. J. A* **56**, 15 (2020), arXiv:1908.04952 [astro-ph.HE].
- [68] S. Bernuzzi *et al.*, *Mon. Not. Roy. Astron. Soc.* (2020), 10.1093/mnras/staa1860, arXiv:2003.06015 [astro-ph.HE].
- [69] T. Dietrich and M. Ujevic, *Class. Quant. Grav.* **34**, 105014 (2017), arXiv:1612.03665 [gr-qc].
- [70] C. J. Krüger and F. Foucart, *Phys. Rev. D* **101**, 103002 (2020), arXiv:2002.07728 [astro-ph.HE].
- [71] D. Radice, A. Perego, F. Zappa, and S. Bernuzzi, *Astrophys. J.* **852**, L29 (2018), arXiv:1711.03647 [astro-ph.HE].
- [72] M. W. Coughlin, T. Dietrich, B. Margalit, and B. D. Metzger, *Mon. Not. Roy. Astron. Soc.* **489**, L91 (2019), arXiv:1812.04803 [astro-ph.HE].
- [73] M. W. Coughlin, T. Dietrich, S. Antier, M. Almualla, S. Anand, M. Bulla, F. Foucart, N. Guessoum, K. Hotokezaka, V. Kumar, G. Raaijmakers, and S. Nissanke, *Mon. Not. Roy. Astron. Soc.* **497**, 1181 (2020), arXiv:2006.14756 [astro-ph.HE].
- [74] M. Bonetti, A. Perego, M. Dotti, and G. Cescutti, *Mon. Not. Roy. Astron. Soc.* **490**, 296 (2019), arXiv:1905.12016 [astro-ph.HE].
- [75] V. Nedora, S. Bernuzzi, D. Radice, A. Perego, A. Endrizzi, and N. Ortiz, *Astrophys. J.* **886**, L30 (2019), arXiv:1907.04872 [astro-ph.HE].
- [76] V. Nedora, F. Schianchi, S. Bernuzzi, D. Radice, B. Daszuta, A. Endrizzi, P. Aviral, A. Perego, and F. Zappa, “Mapping dynamical ejecta and disk masses from numerical relativity simulations of neutron star mergers,” (2020).
- [77] T. Dietrich, M. Ujevic, W. Tichy, S. Bernuzzi, and B. Brügmann, *Phys. Rev.* **D95**, 024029 (2017), arXiv:1607.06636 [gr-qc].
- [78] T. Damour and A. Nagar, *Phys. Rev.* **D80**, 084035 (2009), arXiv:0906.0096 [gr-qc].
- [79] M. Favata, *Phys. Rev. Lett.* **112**, 101101 (2014), arXiv:1310.8288 [gr-qc].
- [80] D. M. Siegel, *Eur. Phys. J. A* **55**, 203 (2019), arXiv:1901.09044 [astro-ph.HE].
- [81] F. Foucart, E. O’Connor, L. Roberts, L. E. Kidder, H. P. Pfeiffer, and M. A. Scheel, *Phys. Rev.* **D94**, 123016 (2016), arXiv:1607.07450 [astro-ph.HE].
- [82] F. Foucart, M. D. Duez, L. E. Kidder, R. Nguyen, H. P. Pfeiffer, and M. A. Scheel, *Phys. Rev.* **D98**, 063007 (2018), arXiv:1806.02349 [astro-ph.HE].
- [83] L. Rezzolla and O. Zanotti, *Relativistic Hydrodynamics* (Oxford University Press, Oxford, 2013).
- [84] F. Foucart, R. Haas, M. D. Duez, E. O’Connor, C. D.

- Ott, L. Roberts, L. E. Kidder, J. Lippuner, H. P. Pfeifer, and M. A. Scheel, Phys. Rev. **D93**, 044019 (2016), arXiv:1510.06398 [astro-ph.HE].
- [85] K. Kawaguchi, K. Kyutoku, M. Shibata, and M. Tanaka, Astrophys. J. **825**, 52 (2016), arXiv:1601.07711 [astro-ph.HE].